Development of a Comprehensive Method to Estimate the Optical, Thermal and Electrical Performance of a Complex PV Window for Building Integration

Xue Li[a *], Yanyi Sun[a], Xiao Liu[a], Yang Ming[a], Yupeng Wu[a, *]

[a] Department of Architecture and Built Environment, Faculty of Engineering, The University of Nottingham, University Park, Nottingham, NG7 2RD, United Kingdom

[*]Corresponding Authors: E-mail addresses: Xue.Li@nottingham.ac.uk (X. Li), Yupeng.Wu@nottingham.ac.uk (Y. Wu).

Abstract:

Increasing concerns over energy consumptions and greenhouse gas emissions in buildings have contributed to the emerging of innovative PV glazing technologies to improve the building energy performance. However, some of these glazing systems have complex structures, making it challenging to investigate their optical, thermal and electrical performance for estimating their energy saving potential in buildings. In this research, a validated Computational Fluid Dynamics (CFD) combined with a ray-tracing model has been developed to accurately predict the solar-optical properties (light transmittance and light absorptance), thermal performance (PV temperature, window temperature, and secondary heat) and electrical performance (power output) of complex PV glazing systems under varying incident angles. A ray-tracing model is developed to calculate the light transmittance of the window as well as the solar energy absorbed by each solid-element and PV cells. To estimate the temperature profile (e.g., PV temperature and window temperature) and secondary heat of the window, ray-tracing results of solar flux absorbed by each layer are transferred into a validated CFD model as boundary conditions. Using the CFD combined ray-tracing calculation illustrated above, the Solar Heat Gain Coefficient (SHGC) of the complex PV window can be obtained. Furthermore, a PV modelling algorithm is developed to predict the power output based on the simulated PV temperature. This procedure is implemented to investigate a Crossed Compound Parabolic Concentrator Photovoltaic (CCPC-PV) window, which serves as an example of a complex PV glazing system in this study. The developed optical, thermal and electrical models have been validated through experimental tests. Additionally, new configurations have been designed to explore the impact of the pitch between adjacent optics on the SHGC and power output of the window. The results show that the original window (1.77 mm-pitch) possesses the maximum

PV temperature of 64.73℃ and the maximum window inside surface temperature of 61.58 ℃ under National Fenestration Rating Council (NFRC) standard. Meanwhile the PV efficiency is 15.21% and the SHGC is 0.463. The SHGC value of this innovative PV window is notably lower than that of a conventional double-glazed window with a SHGC value of 0.813, which reduces the possibility of excessive daylight and solar heat especially during the summer.

Keywords: building integrated PV; complex PV window; solar heat gain coefficient; power output; CFD; ray-tracing.

Nomenclature

Symbols		
α	absorptance	-
τ	transmittance	-
θ	solar incident angle	°
φ	solar azimuth angle	°
λ	wavelength	nm
	also, thermal conductivity of air	W/m·K
η	efficiency	-
δ	temperature coefficient	/℃
c_p	specific heat capacity	J/(kg·K)
A	area	m^2
C	concentration ratio	-
D	distance	M
h	thermal conductance	$W/m^2 \cdot K$
I	current	A
N	fraction of external solar radiation that absorbed by the window then released inward	-
P	electrical power	W
Q	heat flux	W
q	heat flux per unit area	W/m^2
S	volume heat source	W/m^3
T	air temperature	℃
t	pv temperature	℃
Subscripts		
a	air	
e	electric	
	also, exterior	
i	interior	
g	glass	
	also, geometry	

h	heat
in	incident
t	transmitted
r	reflected
op	optical
pv	photovoltaic
sc	short current
st	standard
x, y	cartesian coordinates

Dimensionless numbers

Pr	Prandtl number
Gr	Grashof number

Abbreviation

AM	air mass
PV	photovoltaic
CPV	concentrating photovoltaic
CCPC	crossed compound parabolic concentrator
CCPC-PV	crossed compound parabolic concentrator photovoltaic
CFD	computational fluid dynamics
PS-TIM	parallel slat transparent insulation material
STPV	semi-transparent photovoltaic
SHGC	solar heat gain coefficient
VT	visible transmittance
S2S	surface to surface
WWR	window to wall ratio

1. Introduction

In building energy and daylight simulations, glass windows are typically characterised by three key metrics: U-value, Solar Heat Gain Coefficient (SHGC) and Visible Transmittance (VT) [1-4]. The U-value of a building window is used to indicate the heat loss/gain through it due to indoor and outdoor environmental temperature difference [5]. Therefore, it reflects a window's thermal insulation property, with lower values being preferable for energy efficiency [6]. The VT represents the portion of visible light that passes through a glazing system, which is crucial for indoor daylighting [2, 5]. Traditional window systems often have high U-values, making them the thermal weakest part compared to other building envelope components [7, 8]. Additionally, they can lead to glare issues, especially during the summer because of the high VTs [9]. To address these issues associated with traditional window systems, innovative glazing technologies have been widely developed and investigated in recent decades [10]. For example, Sun et al. [11] investigated the thermal (U-value) and optical (VT) performance of a double-glazed window with Parallel Slat Transparent Insulation Material (PS-TIM). A two-dimensional CFD model was developed to explore the heat transfer into the double-glazed air cavity, both with and without PS-TIM. Additionally, a ray-tracing model was used to analyse the optical transmittance of the systems under different solar incidence angles. The results showed that incorporating a PS-TIM structure between the glass panes can reduce thermal conductance by 35%–46% while maintaining high light transmittance.

The SHGC represents a crucial indicator of window properties that influences the thermal and energy performance of buildings [12]. However, there is a limited body of literature dedicated to estimating it for innovative window designs [13]. This scarcity of studies can be attributed to the complexity and challenges associated with calculating SHGC, especially for windows with complex structures and PV cells. The SHGC is defined as the fraction of external solar radiation that is admitted through a window, both directly transmitted, and absorbed by the window then subsequently conducted, convected, and radiated to the interior of the building (secondary heat) [14-16]. This definition can be expressed as Eq. (1) [17]. Where τ (transmittance) and α (absorptance) are optical properties of layers and N is the fraction of the solar energy absorbed by window layers flowing inwards. Optical properties are all angle (θ) and wavelength (λ) dependent. The SHGC of a window depends not only on the material properties, such as the light transmittance and absorptance, but also the indoor and outdoor environmental conditions, such as air temperature and wind speed [18, 19]. Typical SHGC values for building windows range from 0.2 to 0.7 [5]. The lower a window’s SHCG, the less solar heat it transmits [20], and vice versa. A higher SHGC is important for reducing heating loads in winter but can lead to overheating issues in summer [21]. Therefore, determining the SHGC value of a glazing system is critical for predicting its effects on the annual energy performance of a building fitted with such a glazing system [22, 23].

$$SHGC = \tau(\theta,\lambda) + N \times \alpha(\theta,\lambda) \quad (1)$$

There are various mathematical models have been developed for simulating the SHGC of different kinds of window glazing systems, such as the traditional double-glazed system [24, 25] and PV glazing system [26]. Standard calculation procedures for the SHGC simulation, such as ISO15099 [24], have been developed to calculate simple glazing systems like multi-pane glazing. For some complex glazing systems which cannot be simulated by existing models or the detailed information (e.g., geometry and material properties) is not available for simulation, the experimental method tends to be used. There are two calorimetric methods used for SHGC measurement: indoor calorimeter with solar simulator [16, 27-29] and outdoor calorimeters with or without sun tracking capability [30, 31]. For indoor calorimeter method, Chen [27] measured the SHGC of a selected thin-film Semi-Transparent PV (STPV) glazing using SERIS' indoor calorimetric hot box and solar simulator. Calibrations for the spectrum, irradiance uniformity and temporal stability of the solar simulator were conducted before the actual test. The results showed that when the STPV specimen was connected to a load, the SHGC value was reduced by around 0.01- 0.03. For outdoor calorimeter, Hans et al [30] measured the SHGC of a glazing with venetian blind shading system and the measurement results were also verified using the numerical modelling.

The advantage of the experimental measurement is that the measured sample is treated as a 'black box'. In other words, the structure of the window glazing is not restricted, whether it is a simple traditional system or those with complex optics and PV cells. However, the complicated procedure, time-consuming test as well as the high expense limits its wide use. Recently, the Computational Fluid Dynamics (CFD) combined ray-tracing method to calculate the temperature field and heat loss through different solar systems has been widely used [32-38]. The ray-tracing technique can be used to simulate the detailed light behaviours into the system with complex structures as well as calculate the optical properties, such as the light transmittance and absorption. Then the absorbed solar energy can be input into CFD as one of boundary conditions to simulate the temperature filed and heat flow through the system. For example, Craig [32, 33] investigated the heat loss from a tubular cavity receiver, which can absorb the concentrated solar energy from a parabolic dish at various inclination angles and wind speeds. The solar energy distributed into the receiver was modelled using the ray-tracing software, SolTrace. And then it was transformed as a volumetric source and input into a heat transfer model in CFD. The heat transfer model was validated by an experimental heating test using a blower and burner at its inlet. In the end, heat losses due to the thermal radiation out of the cavity, natural convection and forced convection were presented.

The CFD combined ray-tracing method has also been paid attention by those who investigated window glazing systems. For example, Demanega et al. [39] investigated the temperature field and SHGC value of a complex fenestration system (a triple-glazed window, composed by two sealed cavities and curved commercial blinds on the exterior side) using CFD combined ray-tracing method, which shows the feasibility of using this method to calculate the SHGC of the glazing system with complex structures. **However, the SHGC is more complicated for window glazing system containing solar optics and PV cells, such as the Crossed Compound Parabolic Concentrator Photovoltaic (CCPC-PV) Window. This is because the heat dissipation from PV power generation also participates in the window heat transfer and those inward to the indoor space should be included in the SHGC calculation as shown in Eq. (5.2). The amount of heat released by PV power generation is affected by both of the optical efficiency (η_{op}) and PV conversion efficiency (η_{pv}). The power conversion efficiency (η_{pv}) is affected by the PV temperature especially for those attached to concentrators (PV temperature can reach more than 75 °C [40]).** Therefore, to accurately calculate the SHGC of the glazing system containing complex optics and PV cells, all the above issues need to be solved.

$$SHGC = \tau + N \times \alpha + N' \times \eta_{op} \times (1 - \eta_{pv}) \quad (2)$$

Where, η_{op} is the optical efficiency of the CCPC-PV window. η_{pv} is the PV conversion efficiency. N' is the inward-flowing fraction for heat released by PV.

This study is going to develop a comprehensive model to characterise the optical (light transmittance and light absorptance), thermal (PV temperature, window temperature and secondary heat), and electrical (power output) performance of complex PV window systems at different environmental conditions e.g., due to sun’s altitude and azimuth. A Crossed Compound Parabolic Concentrating Photovoltaic (CCPC-PV) window has been selected as an example for this study. To do this, a framework for combining a ray-tracing model and Computational Fluid Dynamics (CFD) model was proposed and the model development as well as the validation of the ray-tracing model and CFD model were undertaken. Meanwhile the electrical characterisation of the Concentrating PV (CPV) system has been obtained through indoor tests. The validated models were then used to simulate temperature profile (e.g., PV temperature and window temperature) and secondary inward heat of the CCPC-PV window. To accurately predict the system output, the PV conversion efficiency was updated based on the simulated PV temperature. Finally, the SHGC and power output (obtained in this study) as well as the U-value and light transmittance (obtained in our recent work by Li et al (2023) [41]) of the CCPC-PV window and its various designs were presented and compared to a similar structured double-glazed system.

2. Research methodology

To accurately predict the optical (light transmittance and light absorptance), thermal (PV temperature, window temperature and secondary heat) and electrical (power output) performance of the glazing system containing complex structures and PV cells, such as the CCPC-PV window, this section provides a procedure based on the CFD combined ray-tracing method as described in Fig. 1. A ray-tracing model was developed and validated in **Section 2.2** to simulate the light transmittance of the CCPC-PV window as well as the solar energy absorbed by each solid-element and PV cells. To estimate the heat released by PV power generation for inputting into a CFD model for window thermal characterisation later, an electrical test was conducted in **Section 2.3** to obtain the electrical characteristics of the PV cell within the CCPC-PV window, such as the PV conversion efficiency at standard test condition (1000 W/m^2, AM 1.5, 25 °C) and temperature coefficient. In the end, a CFD model was established and validated in **Section 2.4**. The results from the ray-tracing simulation and electrical tests, such as the solar energy absorbed by each element into the CCPC-PV window and the heat released from PV power generation were input into the validated CFD model as boundary conditions to obtain the temperature profile (e.g., PV temperature and window temperature) and secondary heat of the CCPC-PV window. The power output of the CCPC-PV window was calculated from the solar energy incident on the PV surfaces and the final updated PV efficiency based on the simulated cell temperature. Following National Fenestration Rating Council (NFRC) standard [42], the other boundary conditions for those simulations were determined to obtain the SHGC of fenestration products at normal incidence condition as listed in Table 1.

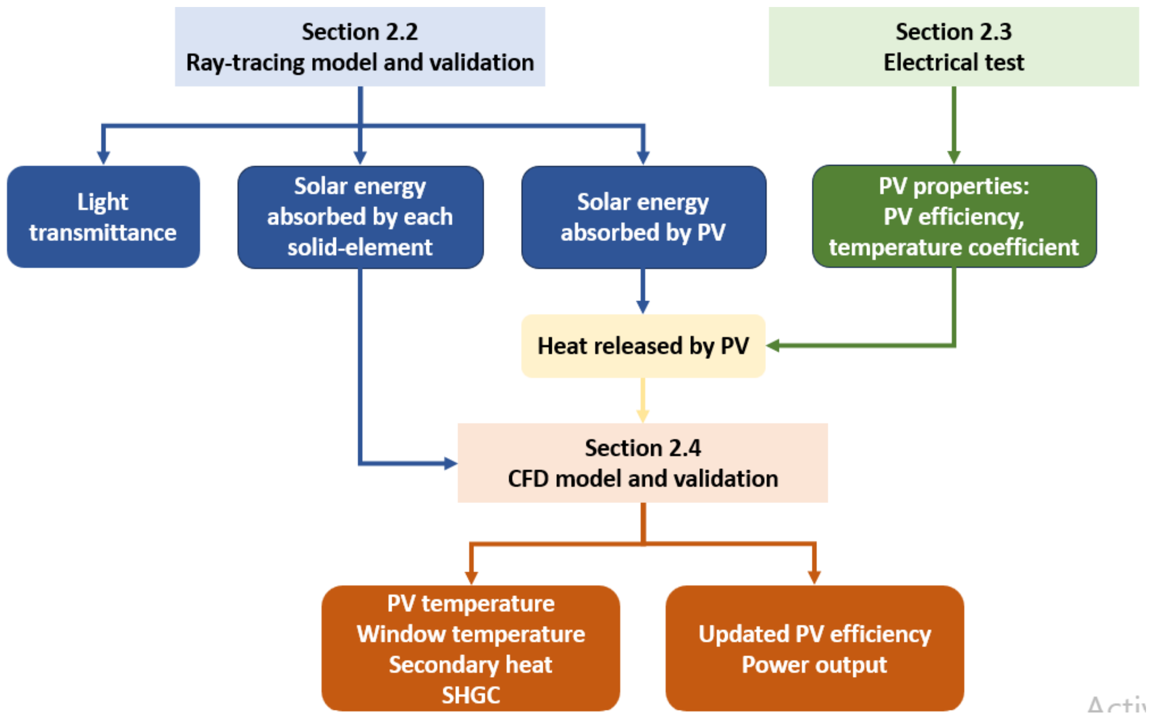

Fig. 1. CFD combined ray-tracing method to predict the optical, thermal and electrical performance of the CCPC-PV window.

Table 1: Boundary conditions for CFD combined ray-tracing simulations.

Standards	NFRC 200
Indoor air temperature	24 ℃
Inside surface heat transfer coefficient	7.7 $W/m^2 \cdot K$
Outdoor air temperature	32 ℃
Outside surface heat transfer coefficient	25 $W/m^2 \cdot K$
Outdoor solar radiation	783 W/m^2

2.1 CCPC-PV window

The window sample with dimensions of 600 mm (height) × 600 mm (width) × 28.06 mm (glazing thickness) × 80 mm (aluminium frame thickness), as shown in Fig. 2 (a), was provided by the University of Exeter, UK [43, 44]. The Crossed Compound Parabolic Concentrator Photovoltaic (CCPC-PV) window consists of 81 3×3 CCPC-PV modules (Fig. 2 (b)) arranged in a matrix of 9×9 sandwiched between two 4mm-thick glass panes. The cross-sectional view of the CCPC-PV window is shown in Fig. 2 (c) with detailed configuration. From the outer layer to the inter layer, it consists of 4 mm-thick float glass pane top, 1.5 mm-thick silicone encapsulant (Sylgard 184), 18.16 mm CCPC optics (2 mm flat joining layer + 16.16 mm parabolic shaped optics), 0.2 mm-thick Sylgard 184, 0.2 mm-thick crystalline silicon solar cells (1 cm^2 area for each cell) and 4 mm-thick float glass pane bottom. Fig. 2 (d) illustrates the geometry of a single CCPC optic with a geometric concentration ratio of 3.6.

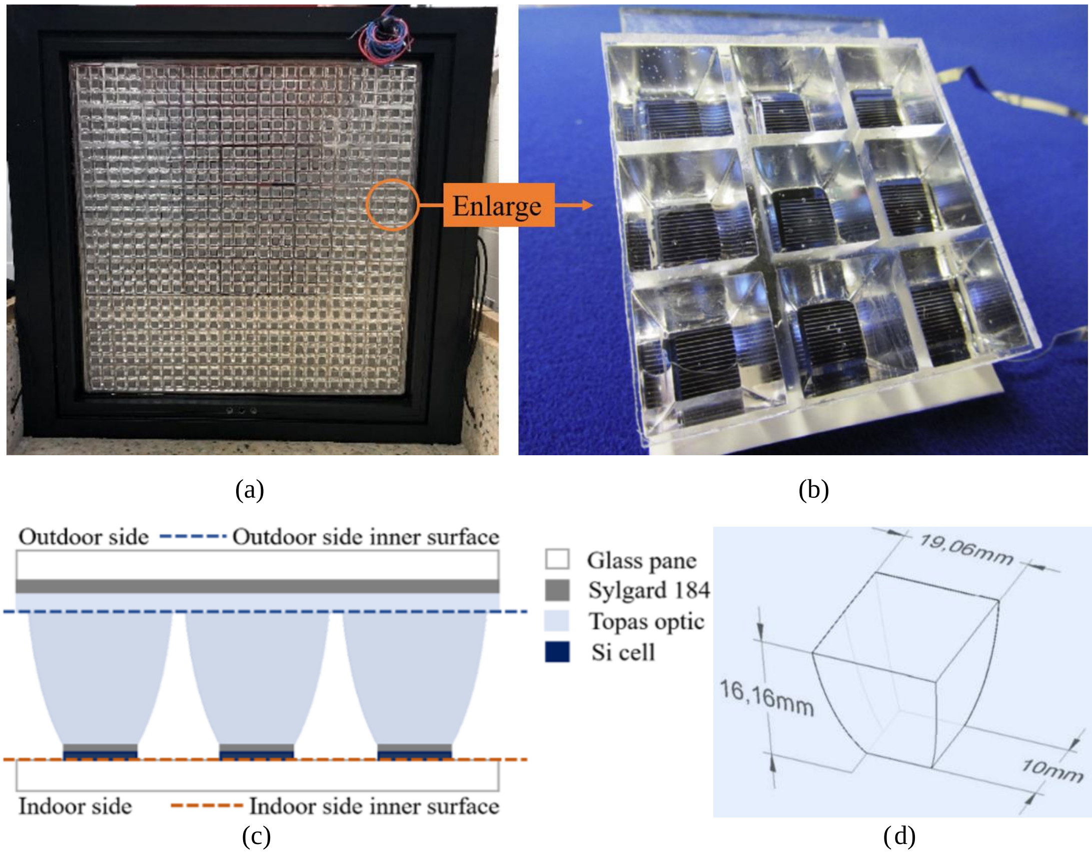

Fig. 2. Pictures of the (a) CCPC-PV window, (b) 3×3 CCPC-PV unit, (c) cross sectional view of the CCPC-PV window with detailed configuration, and (d) schematic sketch of a single CCPC optic.

For the original CCPC-PV window design, the horizontal and vertical pitches between two adjacent CCPC entry apertures are 1.77 mm. In addition to the original design, different horizontal pitches (D_x) and vertical pitches (D_y) were explored to study their effects on the overall window performance.

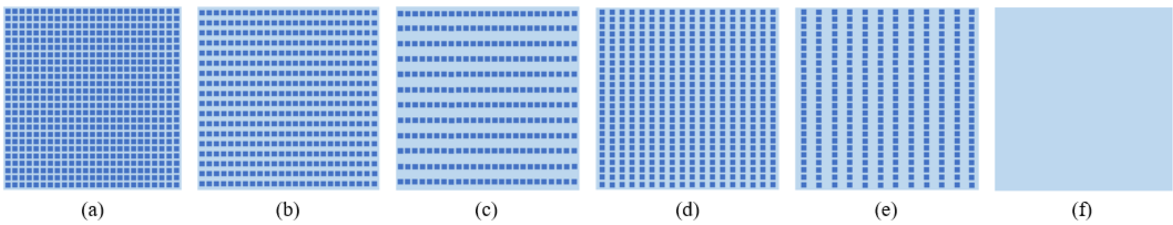

Fig. 3. Different configurations. For left three models, D_x=5 mm & D_y= (a) 5 mm, (b) 15 mm and (c) 30 mm; for right three models, D_y=5 mm & D_x= (d) 15 mm, (e) 30 mm, and (f) reference double-glazed window.

2.2 Ray-tracing model and validation

In this section, a ray-tracing model for the CCPC-PV window was developed (**Section 2.2.1**) and the mode validation (**Section 2.2.2**) was conducted based on small CPV prototypes using spectrometer and solar simulator under indoor conditions. After the model validation, the developed CCPC-PV window model with dimensions of 600 mm (length) × 600 mm (height) × 28.06 mm (thickness) was used to simulate the detailed solar-optical properties including the solar energy absorbed by each solid element and the solar energy incident on PV surfaces. Fig. 4 shows the light flow through a 3×3 CCPC-PV window prototype. The radiation density (q_{in}) was assumed as 783 W/m^2 based on NFRC standard (Table 1). The solar energy absorbed by each element includes A_{ge} for external glass pane, A_s for flat sylgard layer, A_{ft} for flat topas layer, A_c for CCPC optics, A_{gi} for internal glass pane as well as those absorbed by PV cells ($Q_{pv} = Q_e + Q_h$) (Q_e represents the generated power while Q_h represents the released heat). The ray-tracing simulation results for the CCPC-PV window and its various designs can be found in **Section 3.1**, which will be ultimately input into the CFD model in **Section 2.4** for thermal characterisation.

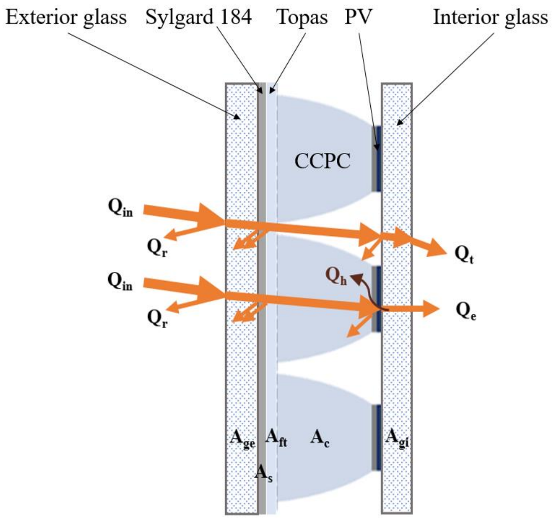

Fig. 4. Light flow through the CCPC-PV window.

2.2.1 Ray-tracing model

This section provides detailed information of the ray-tracing model established using commercial software, TracePro. In the simulation, the incident rays were considered as beam radiation, in other words, all the rays entering the CCPC-PV window contained the same amount of energy and were spaced evenly. Based on the ray independence test as demonstrated in Table 2, 119401 rays were applied on the entry surface of the CCPC-PV window. The solar irradiance was set as 783 W/m^2 (Table 1) for the solar grid source and the spectrum was simplified to be with a single - wavelength of 0.5461μm. The optical properties of the materials used in the CCPC-PV window at single-wavelength spectrum can be found in Table 3.

Table 2. Independent test results of the light source for the ray-tracing simulation.

The number of rays	Total solar radiation incident on window outside surface (W/m^2)		
	0° incident angle	30° incident angle	60° incident angle
29701	1000.3	864.54	501.13
119401	999.72	865.92	499.80
269101	999.12	865.17	499.57
478801	999.79	865.74	499.95
748501	999.49	865.56	499.61
1078201	999.37	865.64	499.30

Table 3. Optical properties of the materials used in the ray-tracing model [11, 44].

Material properties	Float glass	Sylgard 184	Topas (Polyolefin/Zeonex: COC Polymer)
Refraction index	1.52	1.42	1.53
Absorption coefficient (/mm)	0.01	0.01	0.002

Fig. 5 illustrates the symmetry property of one CCPC optic, and it is also the same for the CCPC-PV window. There are four planes of symmetry including the East-West (E-W) plane, North-South (N-S) plane and two diagonal planes (NE-SW and NW-SE) and the angle between the diagonal plane and N-S plane or E-W plane is 45°. Rays from different planes can be transferred into a range from 0° (N-S) to 45° (NE-SW) as all of the incident rays are symmetric about these four planes, which have the same light behaviour into the CCPC optic and CCPC-PV window. In this study, simulations were conducted at different incident angles from 0° to 90° with 10° interval and different plane angles from 0° to 45° with 15° interval.

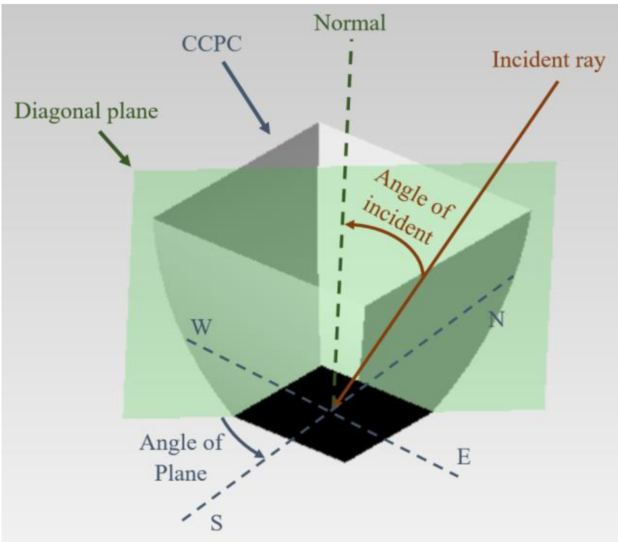

Fig. 5. Incident angle and plane angle of the CCPC optic.

2.2.2 Model validation

In this section, three indoor tests were carried out to validate the ray-tracing model using small CPV prototypes with various devices such as solar simulator and spectrometer. The validated model was then transferred for a full-size CCPC-PV window model with dimensions of 600 mm (length) × 600 mm (height) × 28.06 mm (thickness) to investigate the solar-optical properties of the CCPC-PV window.

2.2.2.1 Validation based on CPV attached with B270 covers

In this section, CPV prototypes with CCPC optic made of glass and topas (Polyolefin/Zeonex: COC Polymer) materials as shown in Fig. 6 (a) and (b) were used to conduct the ray-tracing model validation, respectively. Fig. 6 (c) shows the detailed configuration of these two prototypes. From the outer layer to the inter layer, it is composed of 1.1 mm-thick B270 glass cover, 0.5 mm-thick encapsulant layer (sylgard 182), 16.16 mm-thick CCPC optic, 0.5 mm-thick encapsulant layer, 0.2 mm-thick crystalline silicon solar cell (with area of 1 cm × 1 cm) [43], 1.0 mm-thick encapsulant layer and 1.1 mm-thick B270 glass cover. In addition, a T-type thermocouple was attached at the back of the PV cell to monitor the PV temperature.

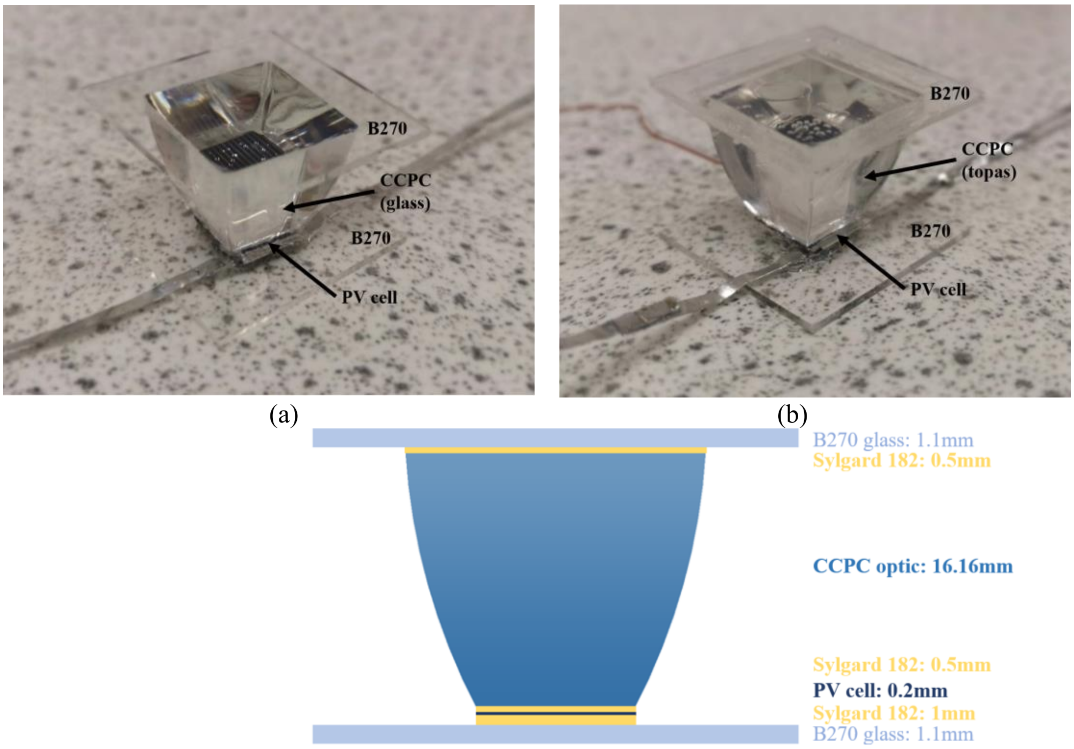

(a) (b) (c)

Fig. 6. Images of (a) glass CPV and (b) topas CPV attached with B270 covers as well as (c) its detailed configuration.

Fig. 7 (a) demonstrates the indoor test setup for ray-tracing model validation. The solar simulator (Oriel Sol3A Model 94063A) from Newport Corporation, which was used to provide the solar radiation with intensity of 1000 W/m^2 over a 152.4 mm × 152.4 mm area, is a class AAA category, and it is suitable for indoor test of PV modules and solar cells. The solar cell into the CPV was linked to a Keithley 2420 source meter unit via a four-wire connection method to measure its current-voltage (I-V) characteristics [45]. Besides, a fan was located behind the CPV prototype to control the cell temperature at around 25 °C, which was monitored by a T-type thermocouple connected to a datalogger DT85. The corresponding ray-tracing model used for the model validation was established as shown in Fig.7 (b). The optical properties of materials into CPV prototypes can be found in Table 4.

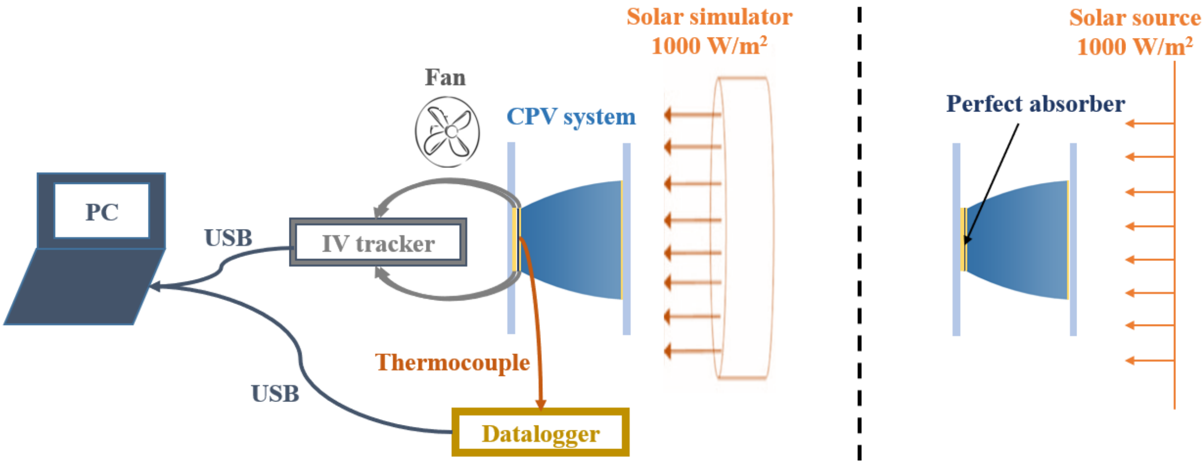

(a) (b)

Fig. 7. (a) Schematic of the indoor test setup and (b) ray-tracing model.

Table 4: Optical properties of the materials used in the ray-tracing model validation [44, 46]

Material properties	B270 glass	Topas (Polyolefin/Zeonex: COC Polymer)	Glass (Crown: CDGM –K)	Sylgard 182
Refraction index	1.523	1.53	1.523	1.41
Absorption coefficient (/mm)	0.0008	0.002	0.00007	0.01

The optical efficiency, which was defined as the ratio of the total solar energy incident on the solar cell to the total incident solar energy on the entry concentrator [47], can be calculated by Eq. (3) and (4). As the ratio of the entry area of the concentrator (A_{in}) and the area of the solar cell (A_{pv}) was defined as a geometric concentration ratio (C_g) [47], the optical efficiency can also be calculated using Eq. (5). Because of the linearity property of the PV cell between the short circuit current output and the incident irradiance [48], the optical efficiency can also be estimated based on Eq. (6) [49, 50].

$$\eta = \frac{Q_{pv}}{Q_{in}} \tag{3}$$

$$\eta = \frac{q_{pv}A_{pv}}{q_{in}A_{in}} \tag{4}$$

$$\eta = \frac{q_{pv}}{q_{in}C_g} \tag{5}$$

$$\eta = \frac{I_{sc,con}}{I_{sc,nocon} \times C_g} \tag{6}$$

Where, Q_{pv} is the solar energy incident on the PV surface, W. q_{pv} is the solar energy incident on the PV surface per PV area (W/m^2). Q_{in} is the solar energy incident on the concentrator entry surface, W. q_{in} is the solar energy incident on the concentrator entry surface per entry surface area (W/m^2). C_g is the geometric concentration ratio, 3.61 for the CCPC optic. $I_{sc,con}$ is the short circuit current of the PV cell attached with a concentrator, A. And $I_{sc,nocon}$ is the short circuit current of a bare PV cell, A.

The measurement results including the short circuit current of CPV prototypes and a bare PV cell (same electrical characteristics with those used in CPV prototypes) under the same cell temperature (25 °C) are listed in Table 5. Using Eq. (6), the optical efficiency was calculated as 82.0% and 80.2% for those attached with glass- and topas-optic, respectively. The ray-tracing results show that the incident energy on the PV surface is 3344.8 W/m^2 and 3195.2 W/m^2 for those attached with glass- and topas-optic, respectively. Using Eq. (4), the corresponding optical efficiency was calculated as 92.5% and 88.6%. The optical efficiency calculated based on indoor test results is 10.5% and 8.4% lower than that from ray-tracing simulation results. This large deviation might result from the thick encapsulant connection/optical bond between individual components causing optical loss. To be more specific, the sylgard between the front cover and optics, and that at the front and rear of solar cell might cause rays near borders to escape from the system due to similar refractive index between the CCPC optic and encapsulant. Further investigation about the losses is going to be discussed in **Section 2.2.2.2**.

Table 5: Optical efficiency of glass CPV and topas CPV (attached with B270 covers) calculated based on indoor test results and ray-tracing results.

PV systems	**Indoor test**		**Ray-tracing simulation**	
	Measured I_{sc}(mA)	Optical efficiency (%)	Incident irradiance on PV(W/m^2)	Optical efficiency (%)
Glass CPV with B270 cover	111.3	82.0	3344.8	92.5
Topas CPV with B270 cover	108.0	80.2	3195.2	88.6
Bare PV cell	37.3	-	1000	-

2.2.2.2 Validation based on CPV

To reduce errors leading to the above large deviation between the indoor test results and ray-tracing results, two B270 glass covers as well as the encapsulant connections between the CPV unit and two covers were removed and only a glass CPV (optics bonded to the PV) and topas CPV as shown in Fig. 8 were used to conduct the validation, respectively.

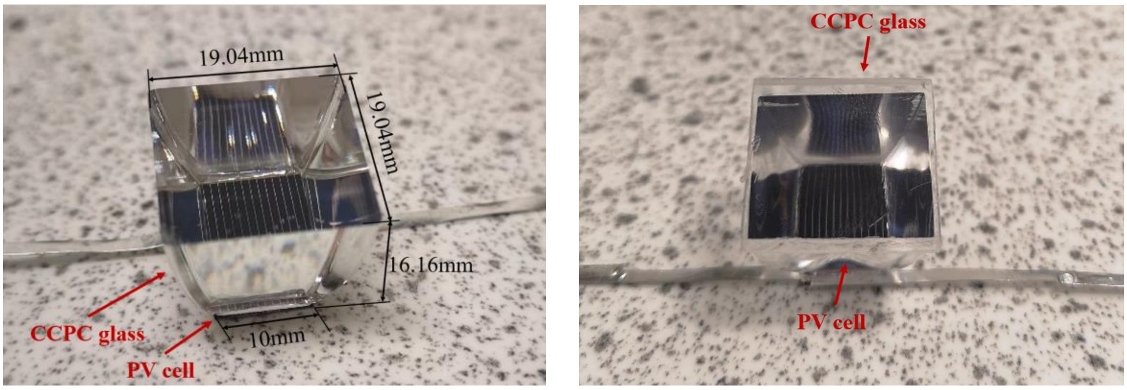

(a) (b)

Fig. 8. Images of a (a) glass CPV and (b) topas CPV.

The indoor test results show the short circuit current of 116.3 mA for glass CPV and 112.3 mA for topas CPV under 1000 W/m^2 solar radiation and 25 °C PV temperature, respectively. Based on above indoor test results, the optical efficiency is 86.4% for glass CPV and 83.4% for topas CPV, respectively. From ray-tracing simulation for similar design, it was obtained that the solar energy incident on the PV surface is 3370.3 W/m^2 for the glass CPV and 3216 W/m^2 for the topas CPV. The optical efficiency is 93.4% and 89.2% for glass CPV and topas CPV, respectively.

Table 6 summarises the optical efficiency obtained based on the indoor test results and ray-tracing results. The optical efficiency calculated based on the indoor test results is 7.0% (glass CPV) and 5.8% (topas CPV) lower than that calculated based on the ray-tracing results. Compared with the results in the last section, the deviation between indoor test results and ray-tracing results becomes smaller (from 10.5% to 7.0% for glass CPV and from 8.4% to 5.8% for topas CPV). For the ray-tracing simulation, the optical efficiency does not consider losses associated with the solar cell, such as the non-uniform energy distribution at the solar cell surface, series resistance losses, etc., which all contribute to a higher efficiency value. For the experimental test, the manufacture error, such as the bubble existing between the PV surface and CCPC optic and the inevitable spreading of the encapsulant to the border of the CCPC optic all result in a lower efficiency value. Therefore, further verification has been carried out based on a single CCPC optic discussed in **Section 2.2.2.3**.

Table 6: Optical efficiency of the glass CPV and topas CPV (without B270 covers) calculated based on indoor test results and ray-tracing results.

PV systems	**Indoor test**		**Ray-tracing simulation**	
	Measured I_{sc} (mA)	Optical efficiency (%)	Incident irradiance on PV (W/m^2)	Optical efficiency (%)
Glass CPV	116.3	86.4	3370.3	93.4
Topas CPV	112.3	83.4	3216	89.2
Bare PV cell	37.3	-	1000	-

2.2.2.3 Validation based on CCPC

Based on the above analysis, the encapsulant (Sylgard 182) connection between the CCPC optic and PV cell is inevitable to increase the optical loss. In this section, only the CCPC optic made of glass as shown in Fig. 9 was used to conduct the model validation. The optical flux transmitted through the CCPC optic was measured at various distances from the exit aperture of the CCPC optic and the measured results were then used to compare the data from the ray-tracing simulation.

Fig. 9. CCPC optic made of glass.

Fig. 10 (a) shows the experimental setup for model validation based one glass CCPC optic. The solar simulator was also used to provide solar radiation (1000 W/m^2 total intensity and 560 W/m^2 visible part). An irradiance probe comprised of an Ocean Optics 100-μm-core-diameter optical fibre and an Ocean Optics CC-3-UV cosine corrector was held against the rear of CCPC optic and connected to an Ocean Optics USB2000+ spectrometer (with a wavelength range of 350–1000 nm and a resolution of 0.5 nm) to detect the light (only visible part) transmitted through the CCPC optic. Then this irradiance probe was located at different distances (4, 5, 7, 10 and 15 mm) from the exit aperture of the CCPC optic to check its effect on the received optical flux. The measurement was repeated four times for each distance and the averaged value was then used to compare the ray-tracing simulation results. The corresponding ray-tracing model was established as shown in Fig. 10 (b). A solar source was used to provide 560 W/m^2 solar radiation (only visible part) to the entry aperture of the CCPC optic. As the light rays emitted from the solar simulator possess a maximum angle of incident of ±5° (half angle) during the indoor test, the ray-tracing simulation was also conducted at 0° and 5° incident angles to mimic the effect of this collimation angle on the validation results. A perfect absorber with 3.9 mm diameter was located at the rear of the CCPC optic to simulate the cosine corrector during the indoor test.

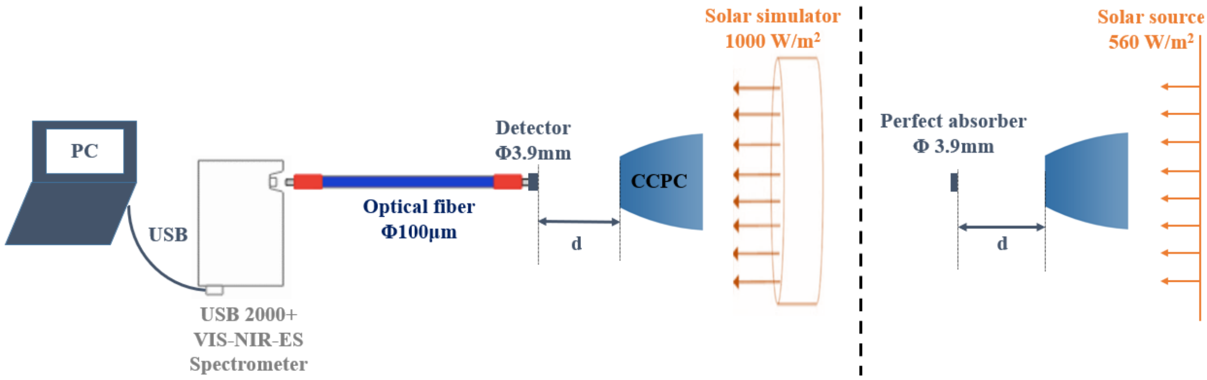

(a) (b)

Fig. 10. (a) Schematic for indoor test setup and (b) corresponding ray-tracing model.

Fig. 11 compares the results of the indoor tests with the ray-tracing simulation for the optical flux received by the probe located at various distances. The ray-tracing simulation shows that the optical flux received by the perfect absorber increases first then decreases from 3.5 mm. It keeps unchanged from 15 mm distance under 0° incident angle. This is because only the directly transmitted solar radiation can be received by the absorber when the distance between the absorber and exit aperture of CCPC optic is larger than 15 mm. The optical flux received by the absorber continuously decreases after the 15 mm distance when the incident angle is 5°. Based on the above ray-tracing results, the irradiance probe was located within 15 mm, such as 4 mm, 5 mm, 7 mm, 10 mm and 15 mm from the exit aperture of the CCPC optic during the indoor test to minimise the effect of the collimation angle on the received optical flux. The validation results show that the deviations between indoor test results and simulation results are all within 4% across all distances.

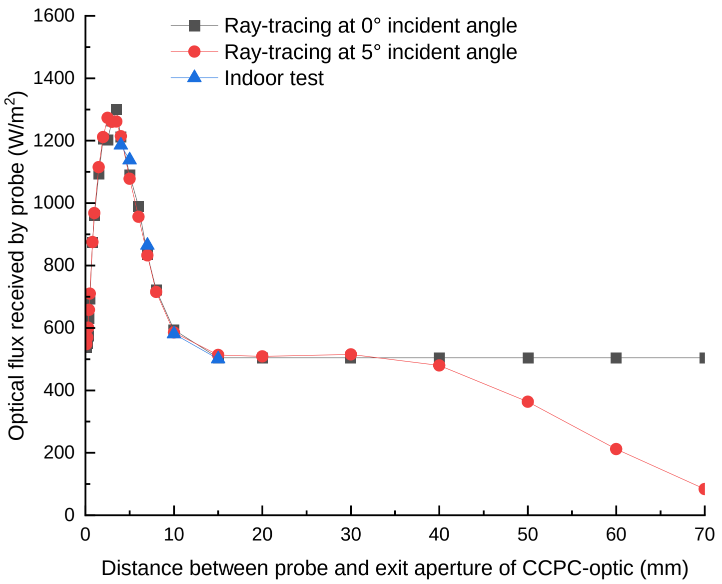

Fig. 11. Comparison between indoor test results and ray-tracing results.

2.2.2.4 Summary of the ray-tracing model validation

This section summarises three validations for the ray-tracing model. For the first validation, the deviation of the optical efficiency calculated based on the indoor test results and ray-tracing results is large (10.5% for glass CPV and 8.4% for topas CPV). This is because the encapsulant connection between the CPV prototype and B270 covers results in large optical loss, which was not considered in the ray-tracing simulation. Through removing the B270 covers as well as the encapsulant connections between B270 covers and CPV units, this deviation can be reduced to 7.0% for glass CPV and 5.8% for topas CPV during the second validation. To further minimise the deviation between the indoor test and ray-tracing simulation, the PV cell as well as the encapsulant connection between the PV cell and CCPC optic were all removed and the (third) validation was conducted using a CCPC optic alone. The validation results showed that the deviations of the optical flux transmitted through the CCPC optic then received by the probe during the indoor test and simulation are all within 4% for all probe positions.

The above prototypes used for the ray-tracing model validations were also chosen to conduct the electrical test for the CPV system as well as the CFD model validation in following sections. The glass CPV and topas CPV without B270 covers (Fig. 8) were used to conduct the electrical tests in the following **Section 2.3** to minimise the effect of the optical loss on the electrical characteristic of the CPV system. Those attached with B270 covers (Fig. 6) were chosen to conduct the CFD model validation in **Section 2.4.2** to ensure the same boundary conditions applied as those used for the CCPC-PV window. The heat released by the PV cell into the CPV prototypes need to be input into the CFD model for model validation. However, there is a large deviation for the solar energy incident on the PV surface obtained from the indoor test and ray-tracing simulation for the CPV units attached with B270 covers. Therefore, both of the indoor test results and ray-tracing results of the solar energy incident on the PV surface were used to estimate the heat released by PV power generation and then input into the CFD model to conduct the model validation.

2.3 Electrical characterisation of CPV

The validated ray-tracing model as described in the last section can be used to simulate the amount of optical flux absorbed by each solid element as well as the PV cells into the CCPC-PV window. However, to estimate the heat dissipation from the PV power generation for inputting into the CFD model (in the next section) for thermal characterisation, the electrical characteristics, such as the PV conversion efficiency at standard test condition (1000 W/m^2, AM 1.5, 25 °C) as well as the temperature coefficient need to be obtained before the CFD simulation. In this section, the glass CPV and topas CPV (without B270 covers) as shown in Fig. 8 were used as samples and the indoor test setup as shown in Fig. 7 was used to conduct the electrical test. Temperature control was used to keep the PV temperature gradually growing up to more than 40 °C. The whole test lasted around 10 minutes and I-V curves of the PV cells were retrieved every 20 seconds.

The simulated I-V and P-V curves under different PV temperatures and 1000 W/m^2 solar radiation are illustrated in Fig. 12 and Fig. 13 for the glass CPV, topas CPV and a bare PV cell. The short circuit current does not show variation in extent for different cell temperatures while the maximum power point and open circuit voltage point shift downwards as the operating temperature of the PV cell increases from the room temperature to more than 40 °C. The open circuit voltage decreases from 0.659 V to 0.631V, from 0.649 V to 0.604 V, and from 0.610 V to 0.582 V for the glass CPV, topas CPV and a bare PV cell during the test. The corresponding maximum power output decreases from 0.059 W to 0.055 W, from 0.053 W to 0.048 W, and from 0.017 W to 0.016 W, respectively.

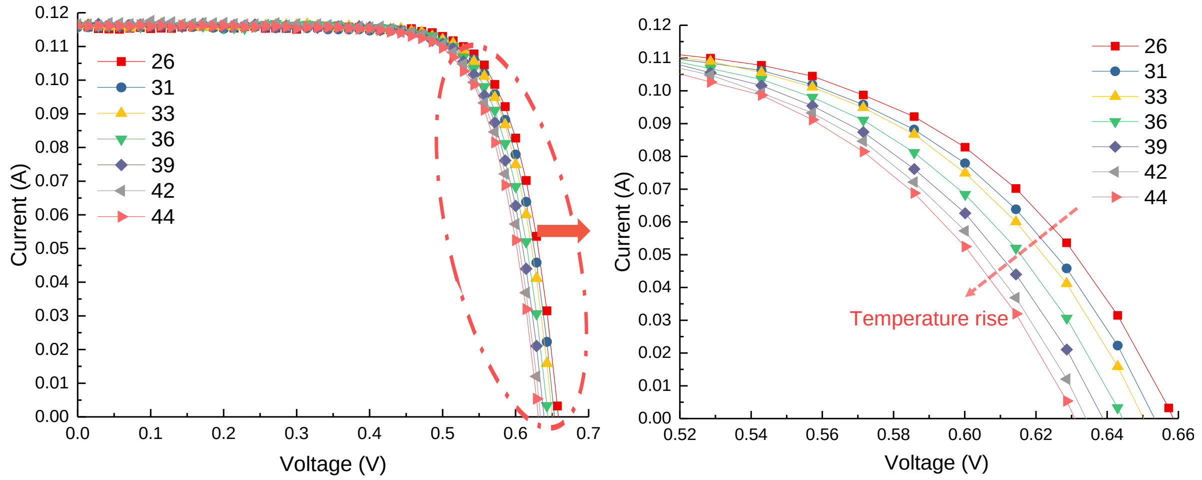

(a)

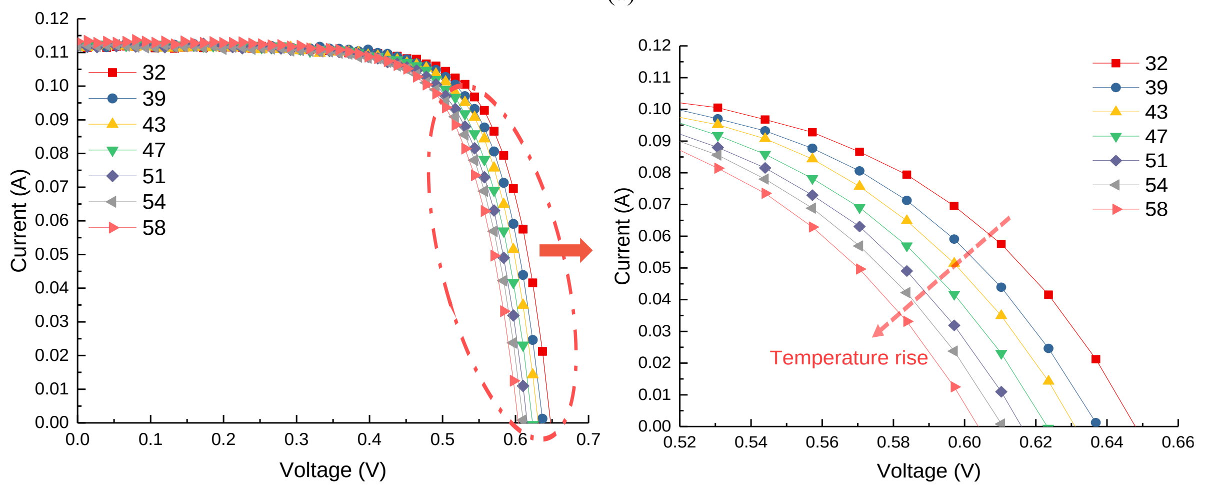

(b)

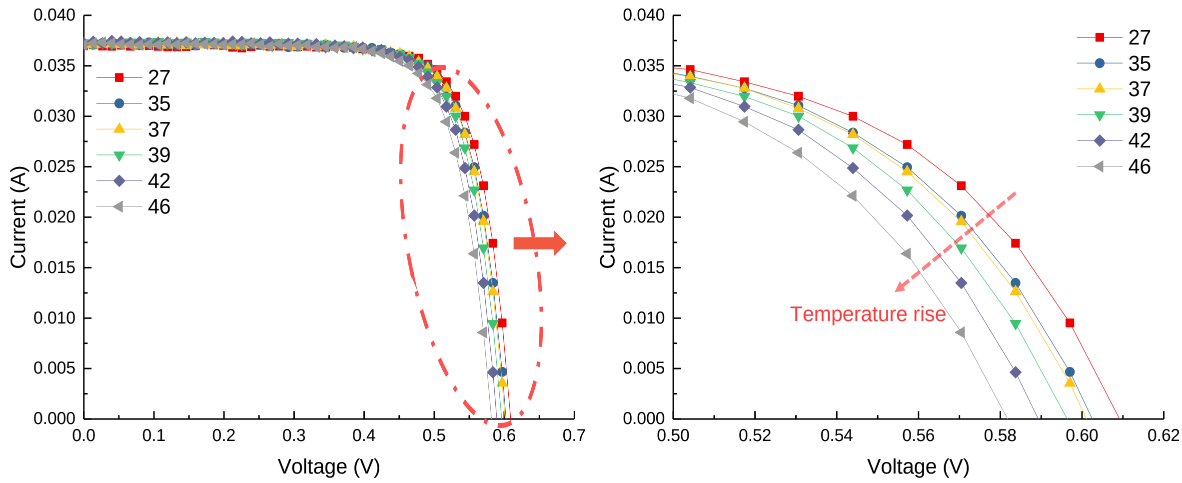

(c)

Fig. 12. I-V curve at 1000 W/m^2 solar radiation with different cell temperatures for (a) glass CPV, (b) topas CPV and (c) PV with no concentrator.

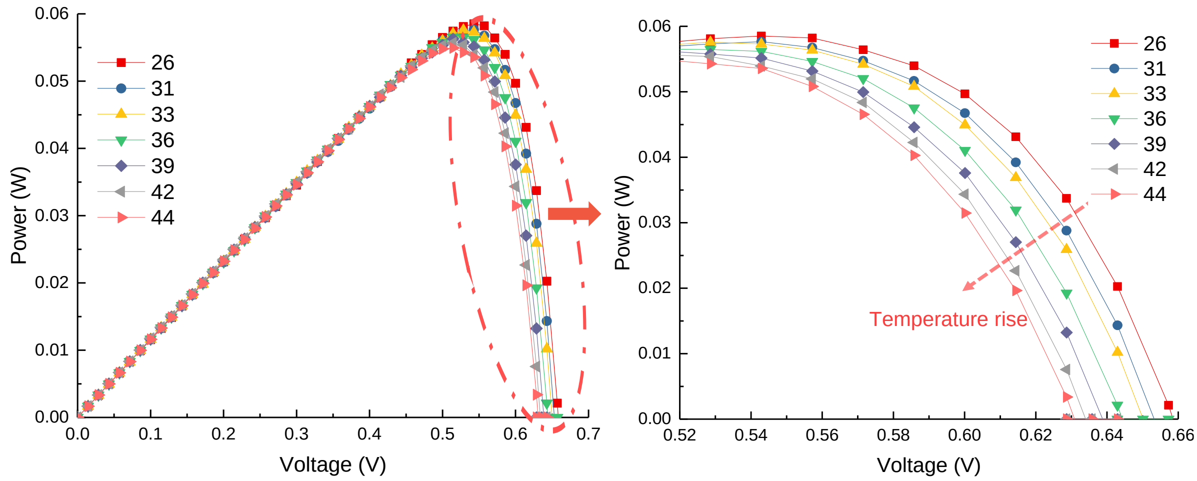

(a)

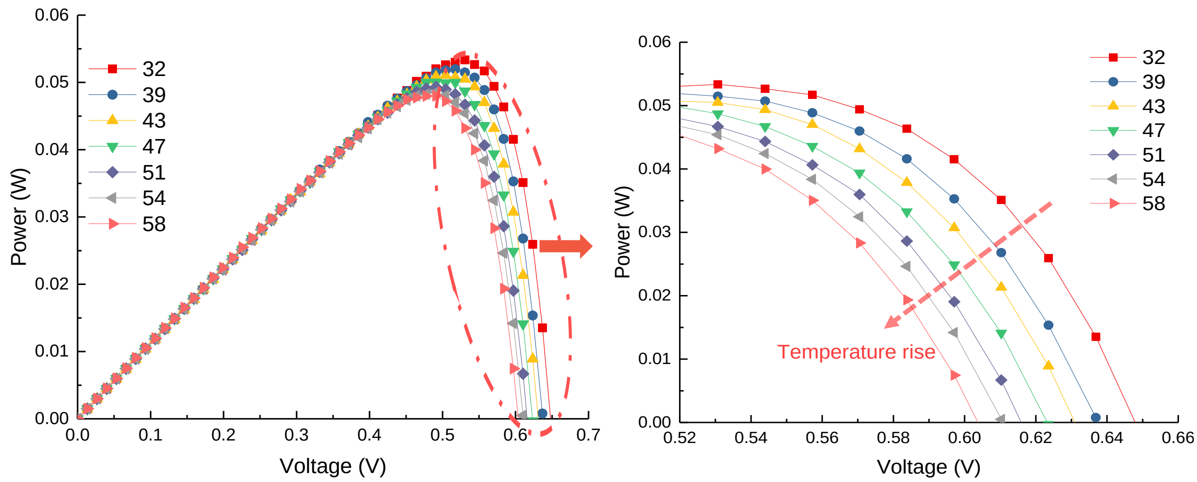

(b)

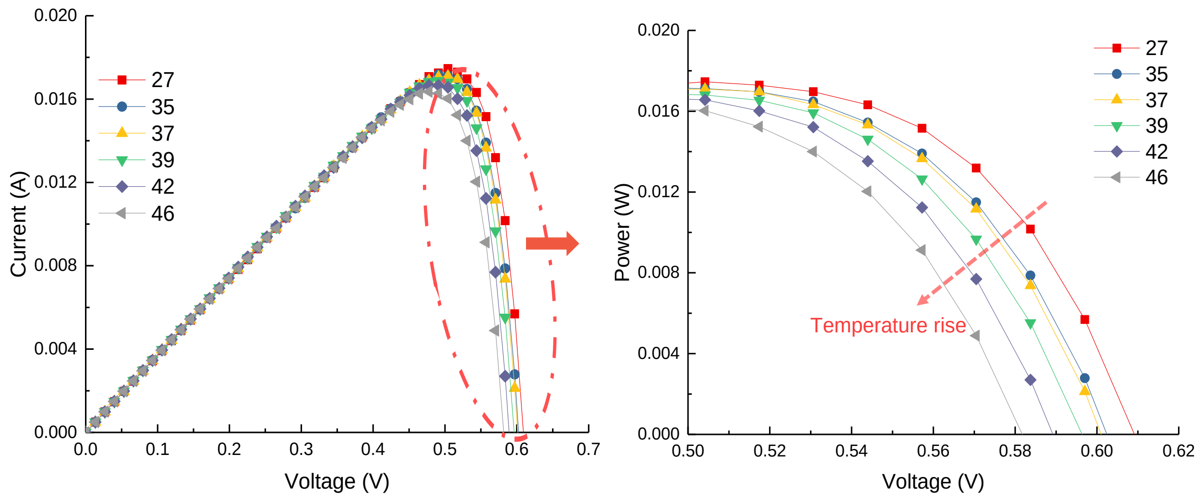

(c)

Fig. 13. P-V curve at 1000 W/m[2] solar radiation with different cell temperatures for (a) glass CPV, (b) topas CPV and (c) PV with no concentrator.

Based on above I-V and P-V curves at different cell temperatures, the relations between PV temperature and short circuit current, open circuit voltage, fill factor and PV efficiency are depicted as shown in Fig. 14. It is obvious that the PV temperature only has a slight effect on the short circuit current for the PV cell with different optics/ no optic attached as mentioned before. The open circuit voltage, maximum power output, fill factor and PV efficiency all decrease linearly with the increase of the PV temperature. As expected, the glass CPV produces the highest maximum power output. Slightly drop of the maximum power output (around 0.005 W) for the topas CPV results from the higher light absorption of the topas material as well as the lower quality optical finish of the PV concentrator. As the glass CPV possesses the higher optical efficiency than that of the topas CPV and the PV efficiency is larger for a higher incident irradiance on the PV surface (optical efficiency), the PV cell attached to a glass concentrator possesses a higher conversion efficiency (19.1%) than that of the PV cell attached to a topas concentrator (18.1%) at 25 °C cell temperature. The corresponding data for a bare PV cell was calculated as 17.6%. The temperature coefficients (δ) were predicted as 0.0031/°C, 0.0039/°C and 0.0034/°C for the PV cell attached to a glass concentrator, topas concentrator and no concentrator, respectively. The PV conversion efficiency (η_{pv}) at specific PV temperature (t_{pv}) can be calculated based on the standard PV conversion efficiency at 25 °C (η_{st}) and temperature coefficient (δ) according to Eq. (7). This relation was used to estimate the heat released by PV power generation for inputting into the CFD model to conduct the thermal characterisation in the next section.

$$\eta_{pv} = \eta_{st}\left(1 + \delta \times \left(25 - t_{pv}\right)\right) \quad (7)$$

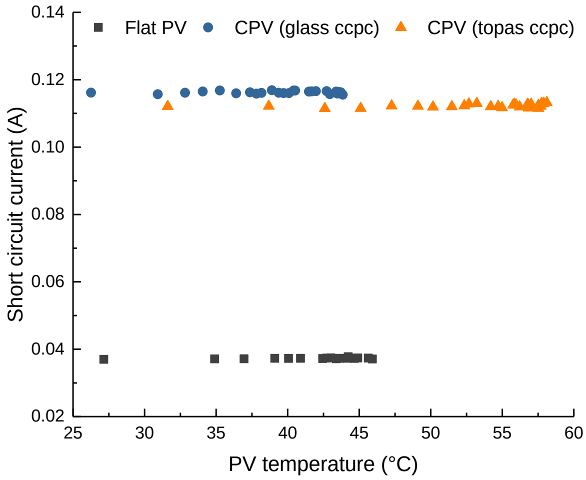

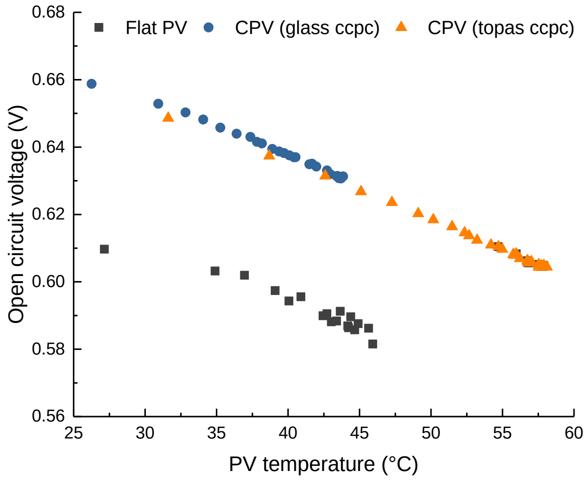

(a) (b)

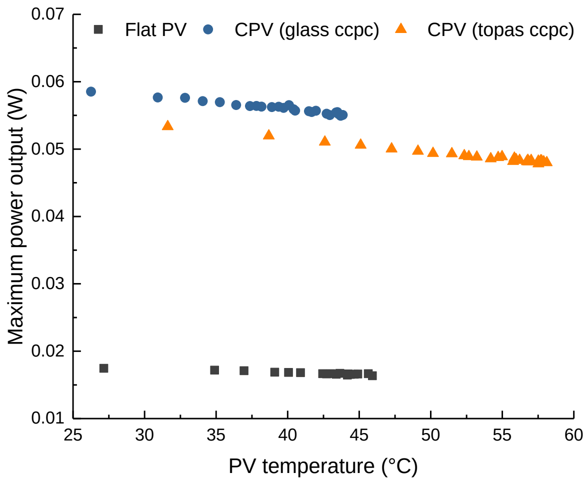

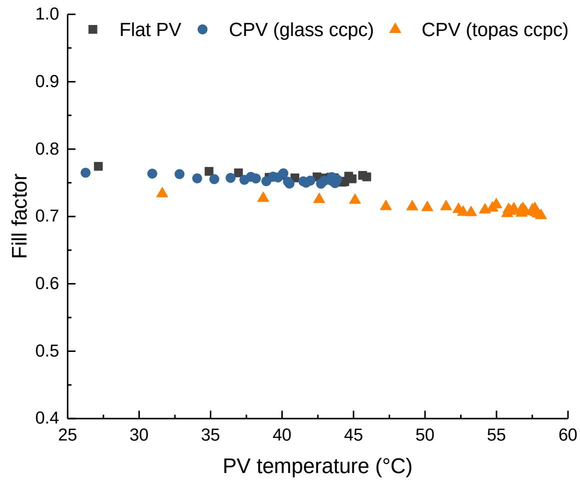

(c) (d)

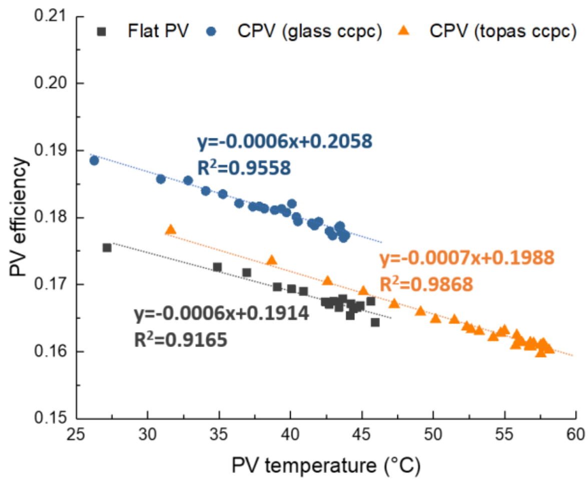

(e)

Fig. 14. Relations between PV temperature and (a) short circuit current, (b) open circuit voltage, (c) maximum power output, (d) fill factor, and (e) PV efficiency.

2.4 Computational fluid dynamics model and validation

Before introducing the CFD model development and validation, the procedure for inputting the simulation results from the ray-tracing model in **Section 2.2** and the measured PV characteristics from the electrical test in **Section 2.3** into the CFD model for thermal characterisation is illustrated in Fig. 15. Based on the ray-tracing simulation, the light transmittance (τ), solar energy absorbed by the CCPC-PV window as well as the solar energy incident on the PV cells can be obtained. For the CCPC-PV window applied to a building, part of absorbed solar energy by each element of the CCPC-PV window and released heat by PV power generation will enter indoor space by convection and radiation, which all contribute to the secondary inward heat. To estimate this secondary heat, those absorbed and released heat were converted as volume heat sources and then input into a CFD model as boundary conditions. The PV conversion efficiency (η_{pv}) was assumed as the value at standard test condition (18%) at the beginning of the simulation to estimate the heat released by PV cells, then it was iterated according to the relation between the simulated PV temperature (t_{pv}) and the PV conversion efficiency (η'_{pv}) obtained through the electrical test in **Section 2.3**. The final updated PV efficiency was used to estimate the system output.

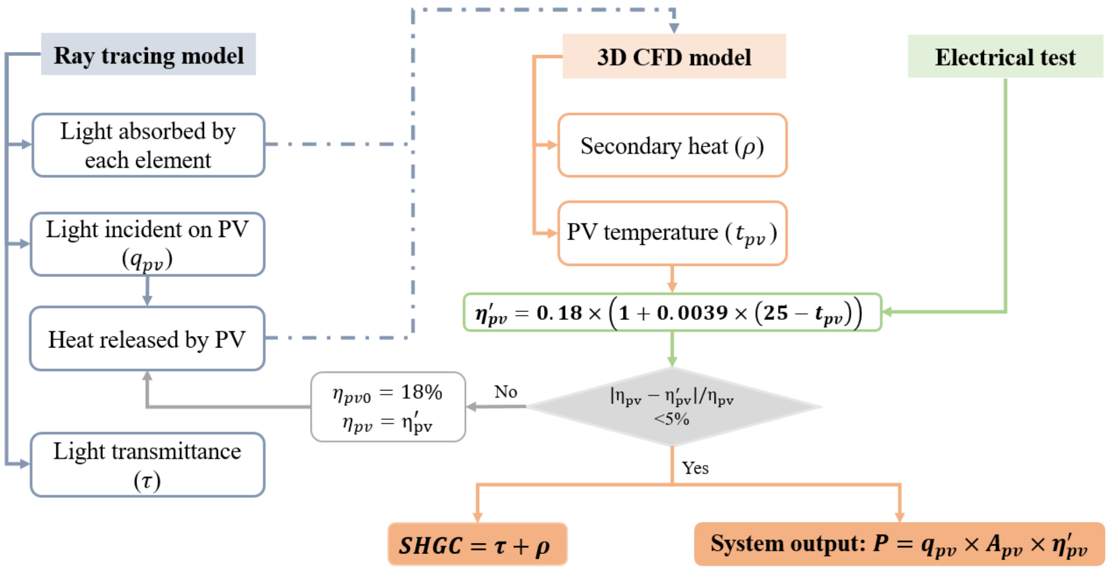

Fig. 15. Procedure for inputting the ray-tracing simulation results and electrical test results into the CFD simulation.

2.4.1 Computational fluid dynamics model

In this section, a numerical simulation model was established to calculate the temperature filed (such as the PV temperature and window temperature) and secondary heat of the CCPC-PV window. Three-dimensional finite volume model was developed in the commercial CFD package FLUENT 19.1. To simplify the CFD simulation process, the following assumptions were made: (1) The enclosure was filled with air with Pr = 0.71, all thermophysical properties (e.g., c_p, λ) of the fluid were assumed to be constant, except for the fluid density and viscosity, which varied with temperature. (2) The flow inside the air cavity formed by CCPC optics keeps laminar as the Grashof (Gr) Numbers never reach the related critical value [51, 52]. (3) The Surface to Surface (S2S) radiation model was used to solve the radiative transfer equation between the internal surfaces. (4) The window geometry with a CCPC-PV matrix of 1×27 rather than 27×27 was used to establish the mesh. The left and right surfaces were set as symmetry while the top and bottom surfaces were set as adiabatic.

The material properties for the developed window model are listed in Table 7, and Fig. 16 shows its boundary conditions. The window indoor and outdoor air temperatures and surface heat transfer coefficients were set based on NFRC standard (Table 1). In addition, the absorbed solar energy (A_{ge}, A_s, A_{ft}, A_c and A_{gi} in Fig. 4) and heat dissipated by PV power generation (Q_h in Fig. 4) were assigned as volume heat sources (S_{ge}, S_s, S_{ft}, S_c, S_{gi}, and S_h) to each solid element in the CCPC-PV window model.

Table 7. Material properties of the CCPC-PV window [11, 43, 44].

Material	Property	Unit	Value
Air	Specific heat capacity	J/kg· K	1005
	Conductivity	W/m· K	0.025
	Expansion coefficient	1/K	0.00353
Topas (Polyolefin/Zeonex: COC Polymer)	Conductivity	W/m· K	0.11
	Emissivity	-	0.84
	Thickness	mm	2(f)+16.16(p)
Glass pane	Conductivity	W/m· K	1.4
	Emissivity	-	0.84
	Thickness	mm	4
PV cell	Conductivity	W/m· K	149
	Thickness	m	0.0004
Sylgard 184	Conductivity	W/m· K	0.16
	Thickness	mm	1.5

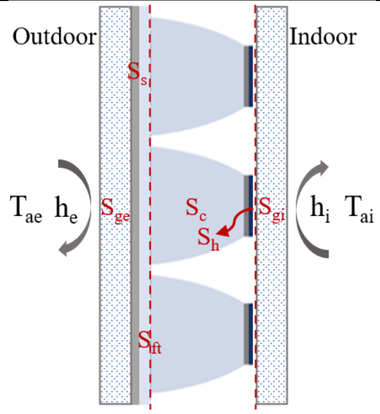

Fig. 16. Boundary conditions for CFD modelling (a 3×3 prototype for an example)

As mentioned before, the SHGC value of the CCPC-PV window can be calculated using Eq. (2). In this equation, the light transmittance (τ) can be obtained through ray-tracing simulation as described in **Section 2,2**, while the remaining of the right side of this equation, which was defined as $\rho = N \times \alpha + N' \times \eta_{op} \times (1 - \eta_{pv})$, can be calculated using Eq. (8).

$$\rho = \frac{Q_{withrad} - Q_{withoutrad}}{Q_{in}} \tag{8}$$

Where, $Q_{withrad}$ is the total heat flux inward to the indoor space through convective and radiative heat transfer for the case of solar radiation from outside, including the heat absorbed by each element, heat released by PV and heat flux driven by indoor and outdoor air temperature difference (thermal transmittance or U-value), W. $Q_{withoutrad}$ is the value for the case of no radiation, the heat flow through the window only due to thermal transmittance (U-value), W. And Q_{in} is the total solar radiation incident on the window outside surface, W. $Q_{withrad}$ and $Q_{withoutrad}$ can be obtained from the CFD simulation for the case of solar radiation from outside (volume heat sources were added into each solid element) and for the case of no radiation, respectively.

2.4.2 Model validation and prediction of power output

Before the model validation, a large number of simulations for iterative convergence and mesh independence were conducted. Iterative convergence was achieved when normalized residuals were less than 10^{-3} for the continuity, and 10^{-7} for momentum and energy equations. The estimated results of the temperature field and secondary heat were calculated from the converged temperature and velocity fields. Mesh independency was achieved when the calculated heat flux was constant as the number of nodes increased. There is total 457564 nodes in this numerical model and the maximum aspect ratio is around 10.

2.4.2.1 Indoor test

Indoor tests were conducted to further check the accuracy of the numerical simulation model. The small glass CPV and topas CPV attached with B270 covers as used for the ray-tracing model validation in Fig. 6 were also employed to conduct the CFD model validation. The validated model was then transferred for a full-size CCPC-PV window model with dimensions of 600 mm (length) ×600 mm (height) ×28.06 mm (thickness) to investigate the thermal performance of the CCPC-PV window. The setup for the model validation is similar to those used for the ray-tracing model validation. However, insulation panels were used to create the adiabatic boundary conditions for the top, bottom and two side surfaces of the CPV with B270 glass covers as shown in Fig. 17. This setup ensures the same boundary condition as the CCPC-PV window installed into building walls. Temperature sensors and hot-wire anemometers were used to monitor the air temperature and wind speed near the test prototype. A thermocouple attached behind the PV cell was used to monitor the PV surface temperature. The fan was not used for the CFD model validation, and the PV temperature was expected to increase continuously until a steady state period. The PV temperature and power output of the CPV prototypes were retrieved during the steady state period, and the measured results were then used to compare with the CFD simulation results for model validation.

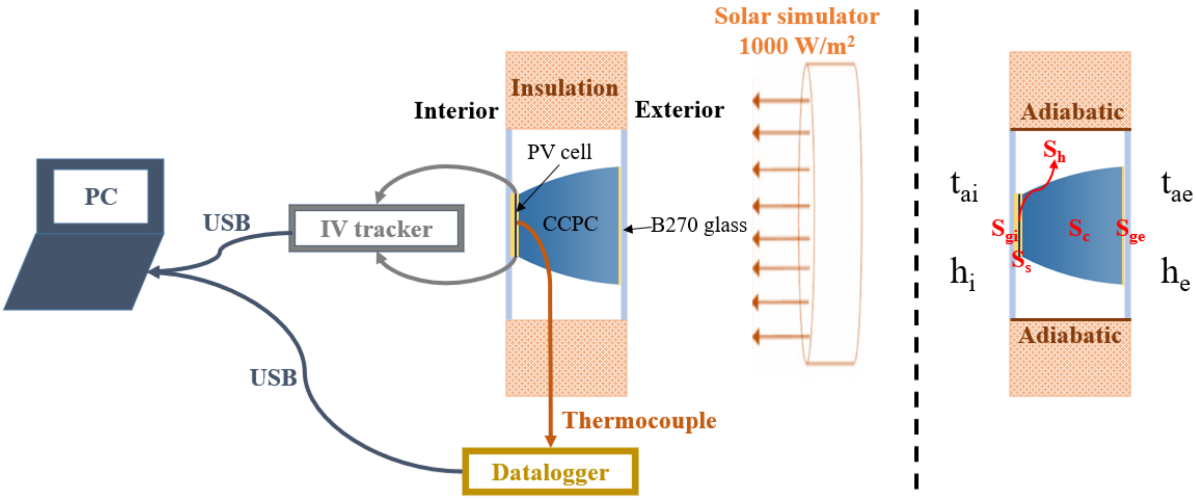

(a) (b)

Fig. 17. (a) Indoor test setup for CFD model validation and (b) boundary conditions for CFD model

2.4.2.2 CFD simulation

Fig. 17 (b) shows the boundary conditions obtained from the indoor test and used for the CFD simulation in a commercial CFD software package FLUENT 19.1 for model validation. Typical heat transfer boundary conditions (air temperature, t_{ai}, t_{ae} and surface heat transfer coefficient, h_i and h_e) and transformed volume heat sources (S_{gi}, S_s, S_h, S_c, and S_{ge}) were applied to the system. As mentioned in **Section 2.2.2** for ray-tracing model validation, there is a large deviation between the indoor test results and ray-tracing results in terms of the optical flux incident on the PV cell. Therefore, the heat released by PV power generation (S_h) was estimated based on the solar energy incident on the PV surface obtained from both of the ray-tracing simulation (q_{pv1}) and indoor test (q_{pv2}). Fig. 18 shows the procedure for inputting these two PV released heat sources terms (S_{h1} and S_{h2}) into the CFD model to conduct the model validation. The solar energy incident on the PV surface was simulated as 3344.8 W/m^2 (glass CPV) and 3195.2 W/m^2 (topas CPV) based on the ray-tracing results (**Section 2.2.2**). The corresponding indoor test results showed that the short circuit current of a bare PV was measured as 0.0373A under standard test condition (1000 W/m^2, AM 1.5, 25 °C) while the short circuit current of the glass CPV and topas CPV was measured as 0.111A and 0.108A under 25 °C cell temperature. Based on PV cell's linearity property between the short circuit current and incident energy on the PV surface, the incident energy on the PV surface was calculated as 2975.9 W/m^2 and 2895.4 W/m^2 for the glass CPV and topas CPV, respectively. The PV efficiency was assumed as 18% at the beginning of the simulation. Therefore, the proportion of the PV released heat

(S_{h1}) on the total solar energy incident on the outside B270 cover was calculated as 30.56% (glass CPV) and 29.41% (topas CPV) and the corresponding proportions were calculated as 27.19% (glass CPV) and 26.65% (topas CPV) for PV released heat, S_{h2}. After all these boundary conditions inputting into the CFD model, the PV efficiency was iterated based on the simulated PV temperature and the final obtained PV temperature (t_{pv1} and t_{pv2}) was compared with the experimental results (t_{pv}). Similar with the CFD model validation, the maximum power output was also calculated based on two groups data and the calculation results (P_1 and P_2) were also verified with the measurement result (P). The detailed information about the thermo-physical properties of the used materials as well as the boundary conditions have been listed in Table 8 below.

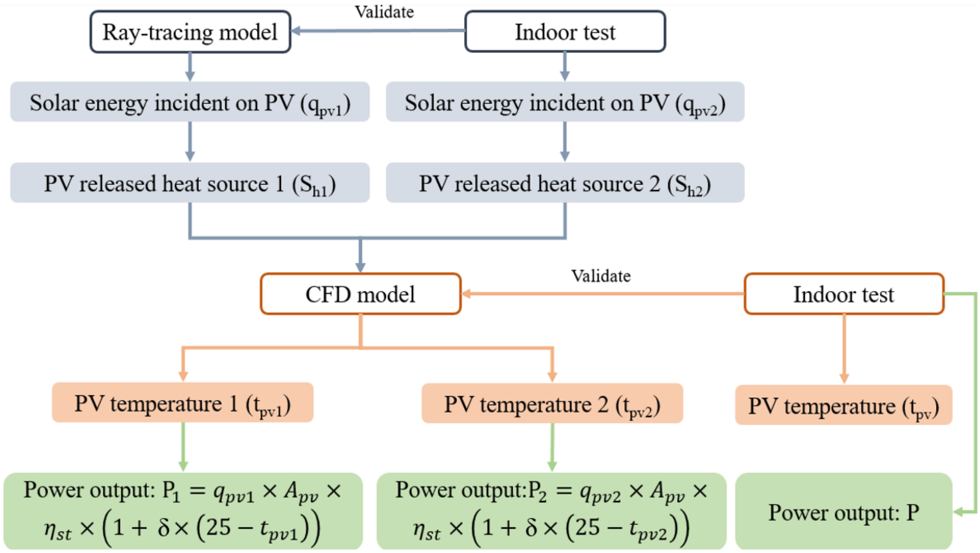

Fig. 18. Procedure for inputting the ray-tracing simulation results and electrical test results into the CFD model to conduct the model validation.

Table 8. Material properties and boundary conditions of the CFD model for model validation.

Air properties: referred in Table 7					
B270 glass properties:					
Density (kg/m^3)	Thermal conductivity (W/m· K)		Heat capacity (J/kg· K)		
2550	1		860		
PV cell properties:					
Density (kg/m^3)	Thermal conductivity (W/m· K)		Heat capacity (J/kg· K)		
2329 [43]	149 [43]		710.08		
Topas (Polyolefin/Zeonex: COC Polymer): referred in Table 7					
Glass (Crown: CDGM –K) properties:					
Density (kg/m^3)	Thermal conductivity (W/m· K)		Heat capacity (J/kg· K)		
2520	1 [44]		820		
Boundary conditions:					
➢ Interior glazing t_{ai} = 302.35 K h_i = 7.7 W/m^2·K	➢ Exterior glazing t_{ei} = 301.75 K h_e = 7.7 W/m^2·K		➢ Top, bottom and two sides end Adiabatic		
➢ Heat source terms					
Components	Exterior B270 (S_{ge})	Sylgard (S_s)	CCPC (S_c)	PV cell (S_{h1}/ S_{h2})	Interior B270 (S_{gi})
Glass CPV	0.11%Q_{in}	0.48%Q_{in}	0.05%Q_{in}	30.56%Q_{in}/27.19%Q_{in}	0.06%Q_{in}
Topas CPV	0.11%Q_{in}	0.47%Q_{in}	1.34%Q_{in}	29.41%Q_{in}/26.65%Q_{in}	0.06%Q_{in}

*Transmittance = 52.59%, reflectance = 9.43% for glass CPV prototype; Transmittance = 52.59%, reflectance = 9.56% for topas CPV prototype.

2.4.2.3 Indoor test results

As for the indoor test, the total testing time is around 4 hours to achieve the steady-state condition and the average measurements of variables (such as air temperature and PV temperature) from two successive measuring periods of 0.5 h after near stability, varied within 1%. The air temperature and PV temperature were averaged based on the last 0.5 hours' steady-state data. Fig. 19 (a) shows that after around 3 hours, the PV temperature and ambient temperature become stable. The temperature of PV cells into the glass CPV and topas CPV were averaged as 54.4 °C and 56.0 °C based on the last 0.5h data as shown in Fig. 19 (b). The interior and exterior air temperatures were averaged as 29.2 °C and 28.6 °C. In addition to the PV temperature, three I-V curves from CPV prototypes were retrieved every 5 minutes during the steady state period and the averaged data from these three curves is shown in Fig. 20. The maximum power output was found as 0.049W and 0.046W for the glass CPV and topas CPV, respectively.

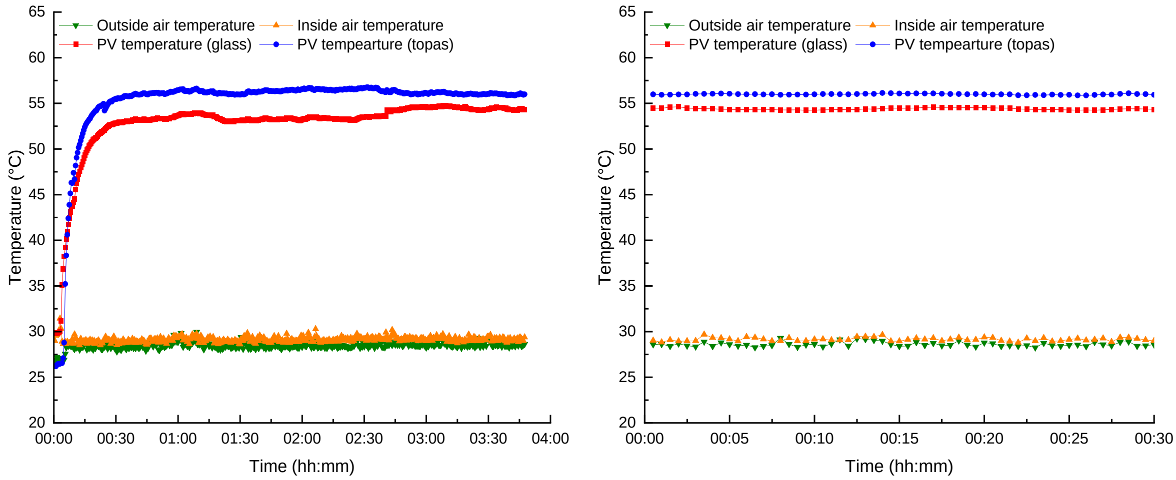

(a) (b)

Fig. 19. Cell temperature and ambient temperature for (a) around four hours' light exposure and (b) last half an hour's light exposure.

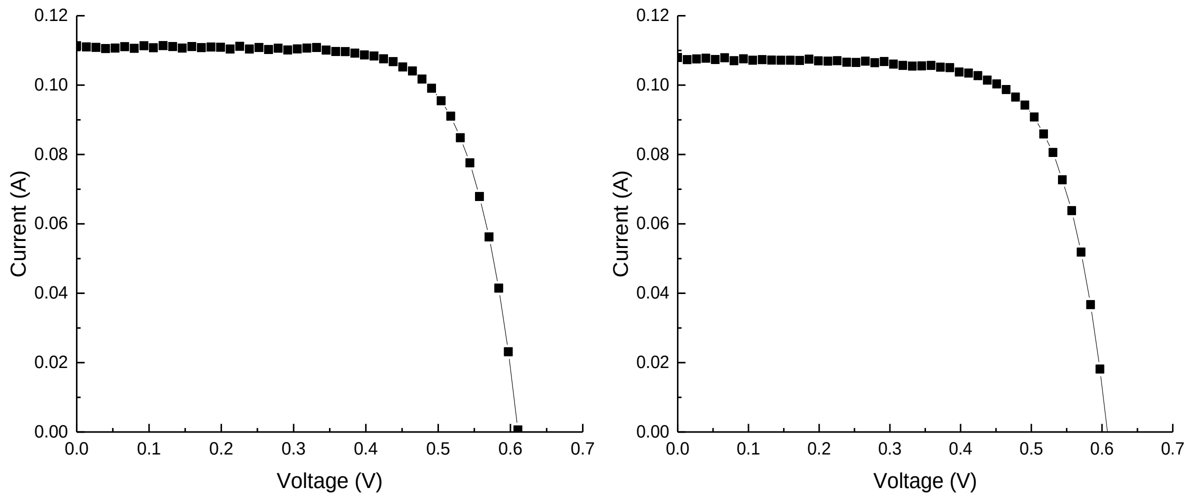

(a) (b)

Fig. 20. I-V curves retrieved from the PV cell into the (a) glass CPV prototype and (b) topas CPV prototype during the steady state period.

2.4.2.4 CFD simulation results

Fig. 21 shows the temperature profile of the glass CPV and topas CPV when the PV released heat calculated from ray-tracing results (S_{h1}) was input into the CFD model. The averaged PV temperatures for glass CPV and topas CPV were simulated as 58.9 ℃ and 64.4 ℃. Fig. 22 shows the temperature profile when the PV released heat obtained from experimental results (S_{h2}) was input into the CFD model. The averaged PV temperatures were calculated as 55.61 ℃ and 61.03 ℃ for glass CPV and topas CPV, respectively.

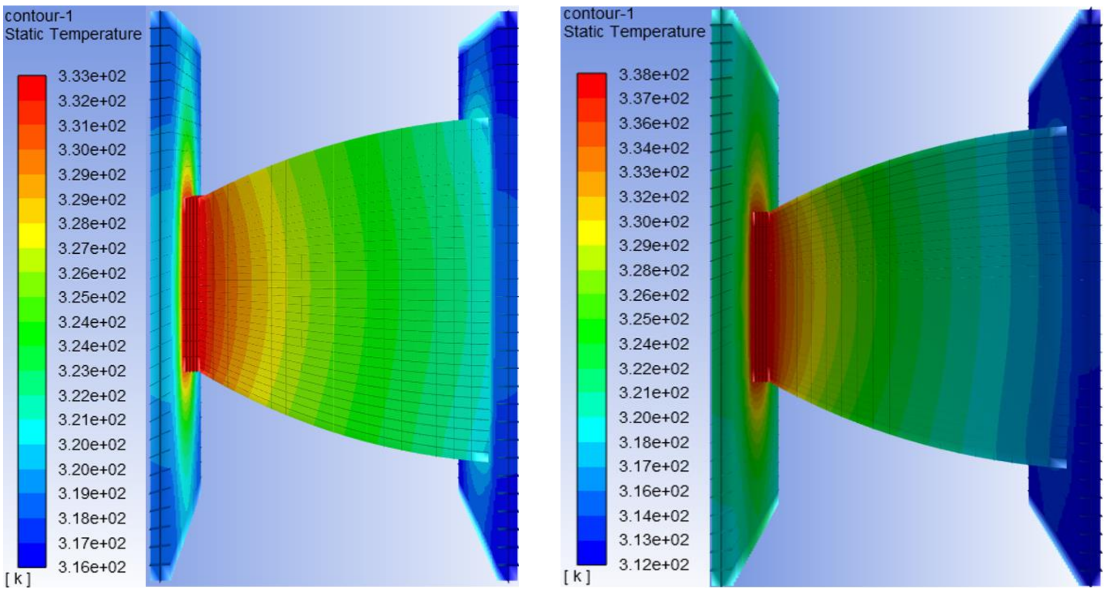

(a) (b)

Fig. 21. Temperature profile of the (a) glass CPV and (b) topas CPV for the PV released heat (S_{h1}) inputting into the CFD model.

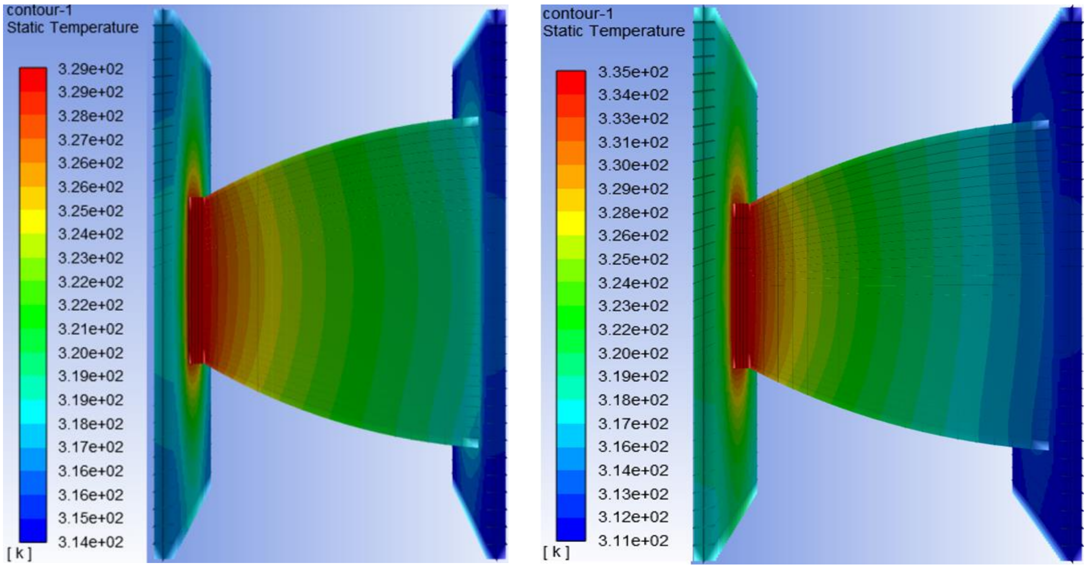

(a) (b)

Fig. 22. Temperature profile of the (a) glass CPV and (b) topas CPV for the PV released heat (S_{h2}) inputting into the CFD model.

Table 9 compares the PV temperature obtained from indoor tests and CFD simulations. There is a large deviation (8.3% for glass CPV and 15% for topas CPV) when the PV released heat (S_{h1}) was input into the CFD model. This is because a large amount of optical loss into the CPV prototype was not considered during the ray-tracing simulation. When this energy term was estimated based on the short circuit current of a bare PV cell and the CPV under same cell temperature (S_{h2}), there is only 2.2% deviation between the indoor test and CFD simulation for the glass CPV. The corresponding deviation for the topas CPV is 8.9%. The PV temperature from the indoor test (56.0 °C) is lower than that from the CFD simulation (61.0 °C). This large deviation is mainly because of the bubble generated between the PV cell and interior B270 cover, which pushes the thermocouple to the edge area of the PV cell.

Table 9. PV temperature of the glass CPV and topas CPV (attached with B270 covers).

CPV systems	**Indoor test**	**CFD simulation**	
		t_{pv1} (δ)	t_{pv2} (δ)
Glass CPV	54.4 °C	58.9 °C (8.3%)	55.6 °C (2.2%)
Topas CPV	56.0 °C	64.4 °C (15.0%)	61.0 °C (8.9%)

'δ' is the deviation between CFD simulation results and indoor test results.

Based on the solar energy incident on the PV surface (Q_{pv}) obtained during the ray-tracing model validation in **Section 2.2.2** and PV temperature (t_{pv}) obtained in this section as well as the electrical test results of the PV efficiency at standard test condition (η_{st}) and temperature coefficient (α) in **Section 2.3**, the maximum power output of the PV cell can be calculated using Eq. (9) and Eq. (10). Considering the large optical loss into the CPV prototypes, the maximum power output was also calculated based on two groups' data. For the first group, the solar energy incident on the PV surface (q_{pv1}) was estimated from ray-tracing simulation results while the PV temperature (t_{pv1}) was obtained based on the CFD modelling when the PV released heat, S_{h1} was input into the CFD model. In the second group, the solar energy incident on the PV surface (q_{pv2}) was estimated from the measured short circuit current while the PV temperature (t_{pv2}) was obtained based on the CFD modelling when the PV released heat, S_{h2}, was input into the CFD model. Based on these two group's data, the maximum power output can be calculated to verify the measured results in Figure 5.17.

$$P_1 = q_{pv1} \times A_{pv} \times \eta_{st} \times \left(1 + \alpha \times \left(25 - t_{pv1}\right)\right) \quad (9)$$

$$P_2 = q_{pv2} \times A_{pv} \times \eta_{st} \times \left(1 + \alpha \times \left(25 - t_{pv2}\right)\right) \quad (10)$$

Where, P_1 and P_2 are the maximum power produced by the PV cell, W. q_{pv1} and q_{pv2} are the solar energy incident on the PV cell, W/m^2. A_{pv} is the cell area, m^2. η_{st} is the PV conversion efficiency under standard test condition. α is the temperature coefficient, /°C. t_{pv1} and t_{pv2} are the PV temperature, °C.

Based on Eq. (9), the maximum power output was calculated as 0.057W and 0.049W for glass CPV and topas CPV, respectively. It was calculated as 0.050W and 0.047W based on Eq. (10). Table 10 compares the power output of the CPV prototypes obtained from indoor tests and calculations. There is a large deviation (16.3% for glass CPV and 6.5% for topas CPV) between the indoor test result and calculation result based on Eq. (9). This is because a large amount of optical loss into the CPV prototypes (with B270 glass covers) was not considered during the ray-tracing simulation, which leads to much higher estimation of incident energy on the PV surface. When the power output was calculated based on Eq. (10), there is only 2.0 % (glass CPV) and 2.2% (topas CPV) deviation between the indoor test result and calculation result.

Table 10. Power output of the glass CPV and topas CPV (attached with B270 covers).

CPV systems	**Indoor test**	**CFD simulation**	
		P_1 (δ)	P_2 (δ)
CPV (glass)	0.049W	0.057W (16.3%)	0.050W (2.0%)
CPV (topas)	0.046W	0.049W (6.5%)	0.047W (2.2%)

'δ' is the deviation between indoor test and calculation based on Eq. (9) and Eq. (10).

2.4.2.5 Summary of the CFD model validation

This section validates the CFD model for the thermal characterisation of the CCPC-PV window based on small CPV prototypes using indoor tests. The PV temperature and power output of the CPV prototypes were measured during the steady state period and the measured results were compared with the corresponding CFD combined ray-tracing results. The validation results showed that there was a large deviation of PV temperature (more than 10%) when the PV released heat estimated through ray-tracing simulation results was input into the CFD model because of the optical loss into the CPV prototype not included in the ray-tracing simulation. When this energy term was estimated based on the experimental results, the deviation becomes smaller (less than 3%). Similar for the power output, there was a large deviation (more than 15%) between the indoor test result and calculation result based on CFD combined ray-tracing method when the solar energy incident on the PV surface was estimated through ray-tracing simulations. When this energy term was estimated through experimental data, this deviation was only 2.0 % for glass CPV and 2.2% topas CPV.

Based on the above analysis, it can be seen that the main reason for causing the deviation of the PV temperature and power output between indoor test results and CFD combined ray-tracing results is because of the optical loss existing into the thick encapsulant connection in the CPV prototypes. This thick encapsulant connection results from the presence of the thermocouple at the back of the PV cell as well as the inexperience of making CPV units. None of these issues exists for the professionally made CCPC-PV window. Therefore, the established numerical simulation model can be used for thermal characterisation of the CCPC-PV window with dimensions of 600 mm (length) × 600 mm (height) × 28.06 mm (thickness).

3. Results and discussion

In this section, the optical, thermal and electrical performance of the CCPC-PV window and its various designs are presented at different incident angles from various planes. The solar-optical properties of the CCPC-PV window for inputting into the CFD model for thermal characterisation, such as the solar energy absorbed by each element and PV cells into the CCPC-PV window are presented first. Then the detailed thermal and energy performance of the CCPC-PV window, such as the PV temperature, window temperature, secondary heat, SHGC and system output are discussed and compared with a similar structured double-glazed system.

3.1 Ray-tracing results

In this section, the solar-optical properties are presented for the original CCPC-PV window first then the results are presented for the system with various designs. The presented data mainly includes the proportion of solar energy absorbed by each solid element and PV cells on the total solar energy incident on the window outside surface. Those absorbed energy terms were then transformed as volume heat sources and input into the CFD model as boundary conditions for thermal characterisation (results can be found in **Section 3.2**).

3.1.1 Solar energy absorbed by original CCPC-PV window

Fig. 23 shows the incident angle of the CCPC-PV window (a 3×3 prototype) and a similar structured double-glazed system. Fig. 24 shows the proportion of each element absorbed solar energy on the total solar energy incident on the window outside surface at different incident angles from various planes. All proportions increase first then decrease as the incident angle increases from 0° to 90° and most of peak values occur between 60° and 80°. A higher proportion occurs at a higher plane angle except for the inside glass layer. Fig. 24 (f) shows the proportion of solar energy incident on the PV surface gradually decreases as the incident angle increases from 0° to 90° and a higher plane angle produces a larger proportion value for incident angle between 40° and 80°.

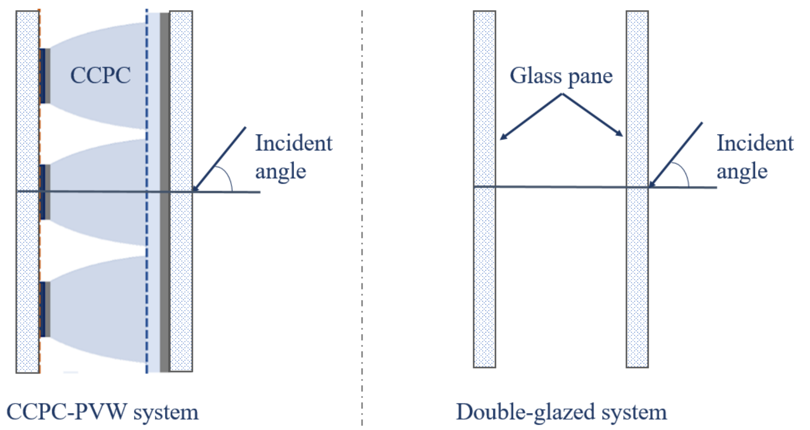

(a) (b)

Fig. 23. Incident angle of the (a) CCPC-PV window and (b) a similar structured double-glazed system.

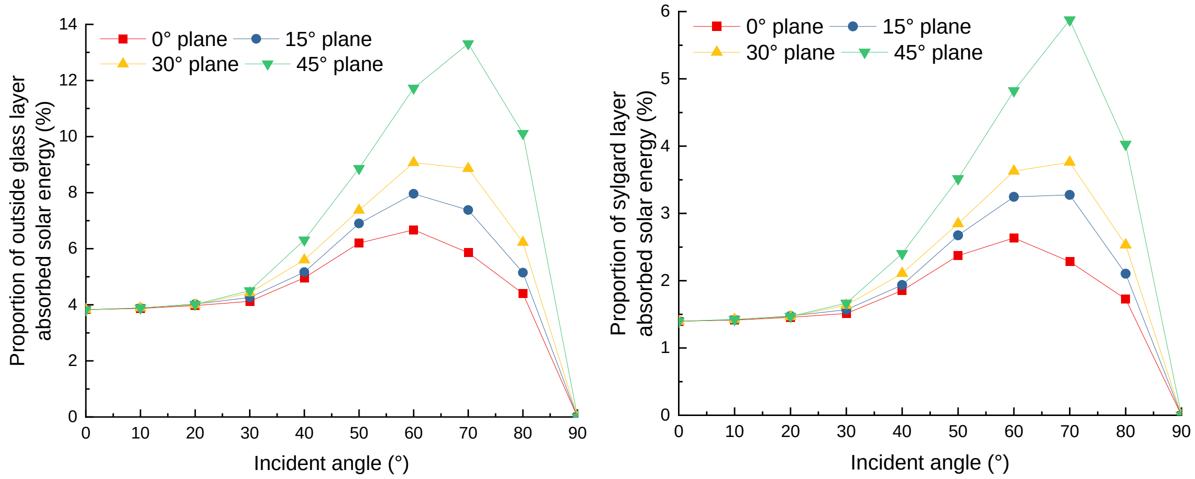

(a) (b)

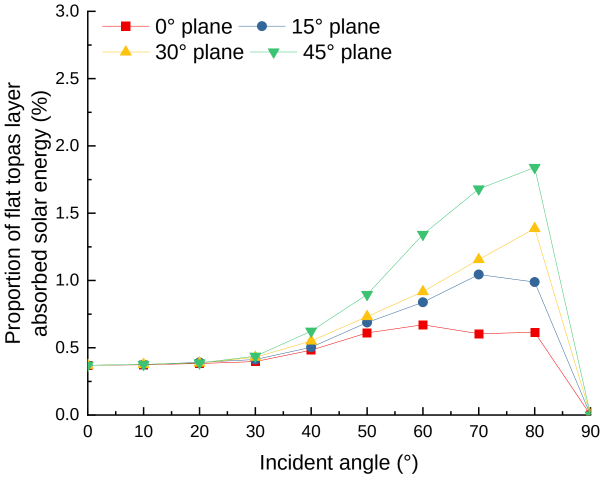

(c)

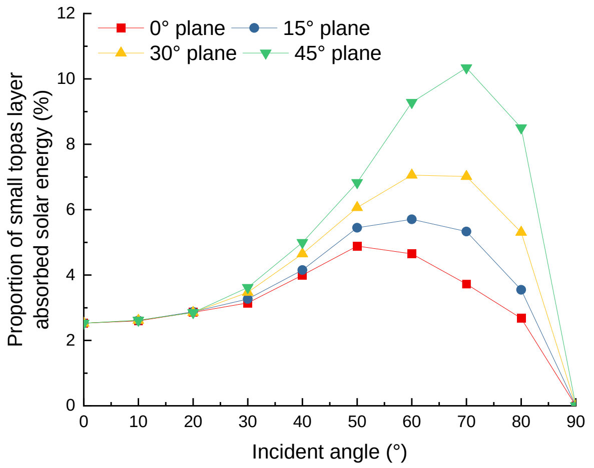

(d)

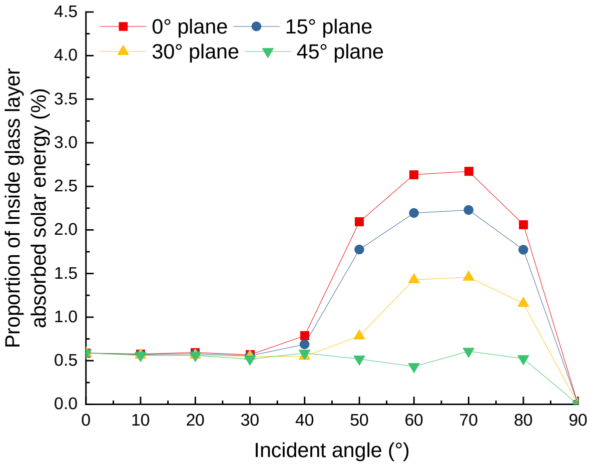

(e)

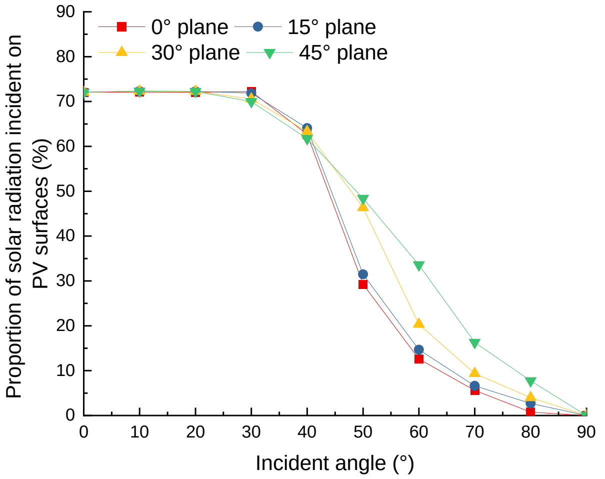

(f)

Fig. 24. Proportion of (a) outside glass layer, (b) sylgard layer, (c) flat topas layer, (d) CCPC optics, (e) indoor glass layer absorbed solar energy and (f) the solar radiation incident on PV surfaces on the total solar energy incident on the window outside surface.

3.1.2 Solar energy absorbed by CCPC-PV window with various designs

This section shows the data for the window with a CCPC-PV structure of various horizontal pitches (D_x) and vertical pitches (D_y) as shown in Fig. 25. Fig. 26 (a), (c), (e), (g), (i) and (k) show the proportions of solar energy absorbed by front three flat layers, CCPC optics, inside glass layer, and PV cells for solar rays from 0° plane while Fig. 26 (b), (d), (f), (h), (j) and (l) show the corresponding proportions for solar rays from 45° plane. With the increase of the pitch between adjacent CCPC optics, the number of PV cells into the window decreases, which results in the decrease of the proportion of incident rays absorbed by PV cells.

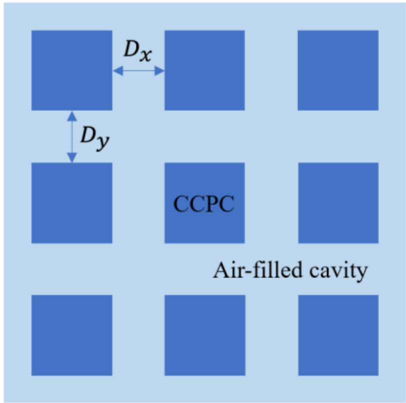

Fig. 25. Horizontal pitch (D_x, mm) and vertical pitch (D_y, mm) between adjacent CCPC optics into a 3×3 CCPC-PV window prototype.

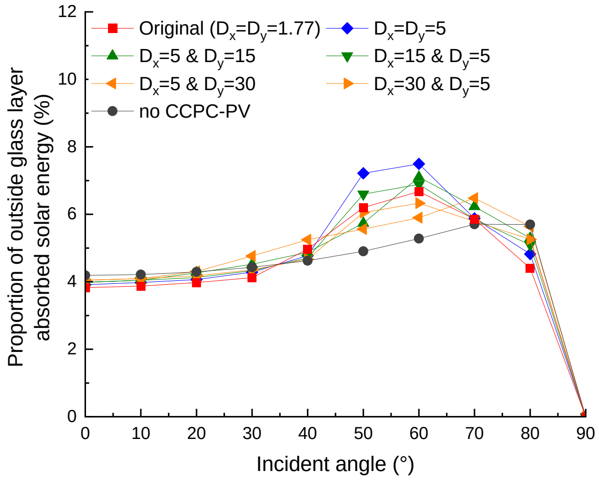

(a) 0° plane

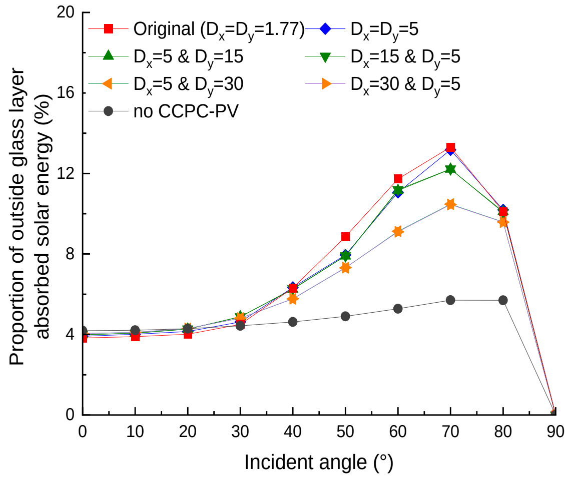

(b) 45° plane

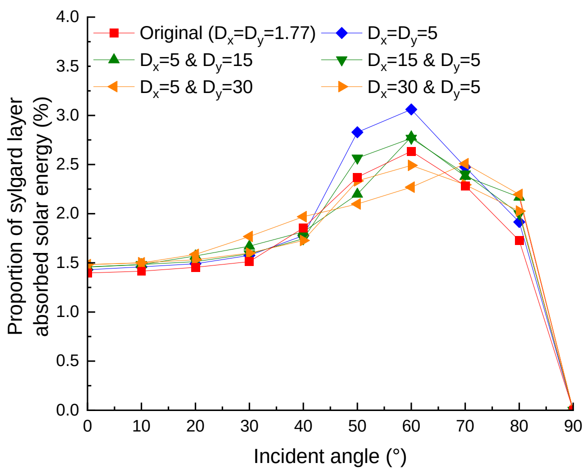

(c) 0° plane

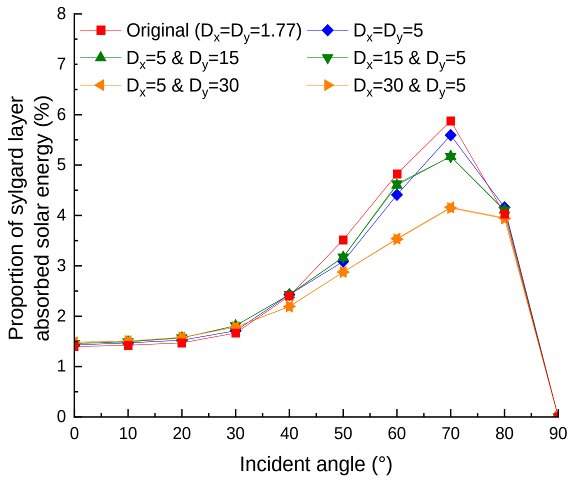

(d) 45° plane

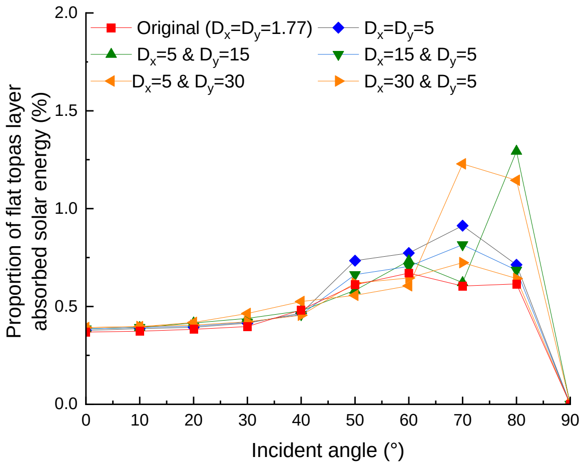

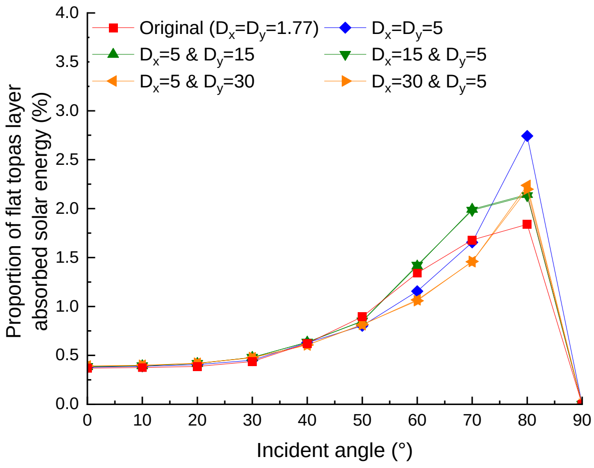

(e) 0° plane (f) 45° plane

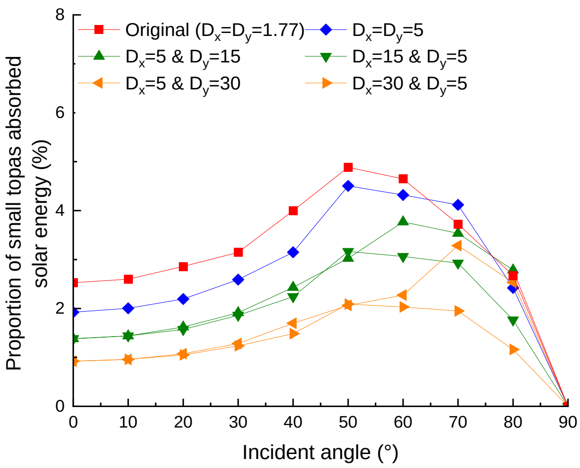

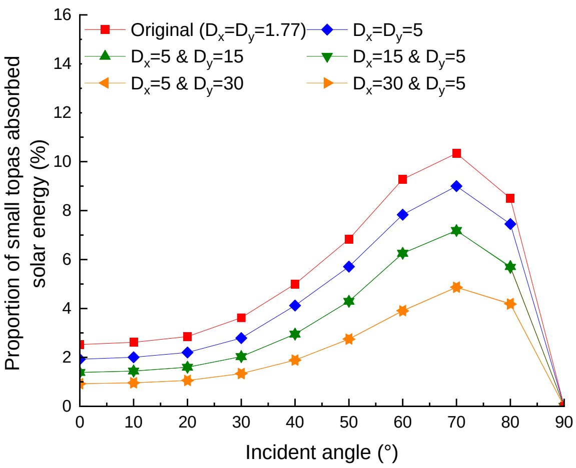

(g) 0° plane (h) 45° plane

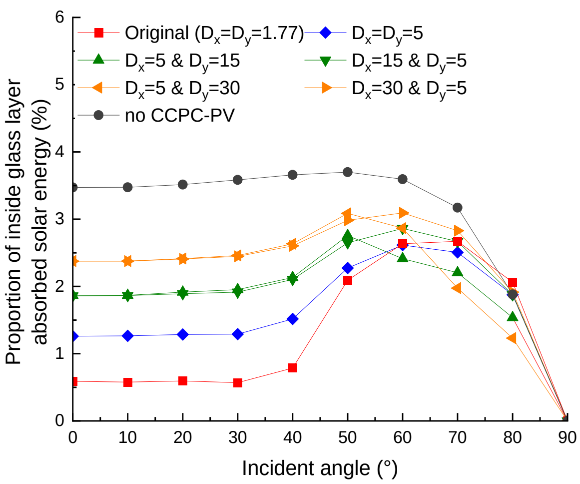

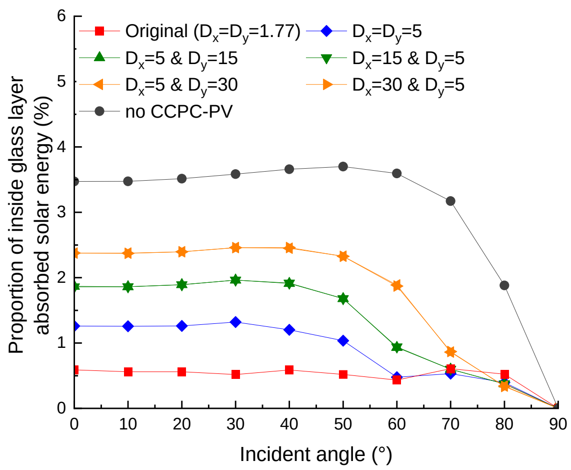

(i) 0° plane (j) 45° plane

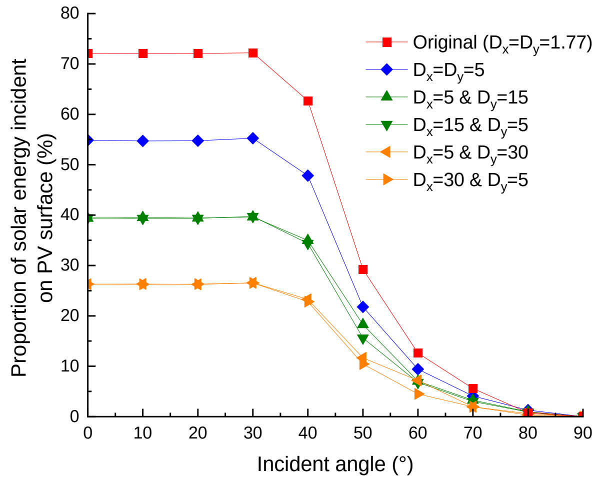

(k) 0° plane

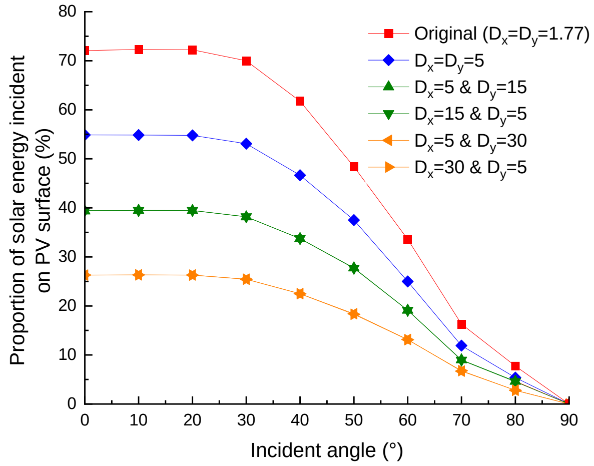

(l) 45° plane

Fig. 26. Proportion of (a) outside glass layer, (c) sylgard layer, (e) flat topas layer, (g) CCPC optics, (i) indoor glass layer, and (k) PV cells absorbed solar energy on the total solar energy incident on the window outside surface for rays from 0° plane, and the corronsponding proportions (b), (d), (f), (h), (j), and (l) for rays from 45° plane (D_x and D_y are horizontal and vertical pitches, mm).

3.1.3 Summary

Based on the ray-tracing simulation results for the original CCPC-PV window, it can be seen that the PV cells into the CCPC-PV window can absorb a large proportion (more than 70% at 0° incident angle) of solar energy incident on the window outside sutrface. While the other solid elements, such as the outdoor glass layer, sylgard layer, flat topas layer, CCPC optics, and indoor glass layer all absorbed less than 15% of total solar energy incident on window outside surface at different incident angles. As the horizontal (D_x) /vertical pitch (D_y) between adjacent CCPC optics increased from 5 mm to 30 mm, the proportion of solar energy incident on the PV surfaces decreased from 55% to 26% (at 0° incident angle) because of the reduced number of CCPC-PV units into the window. The corronspoding proporions for the other solid elements also kept low for these new designed windows. A small portion (less than 18%) of solar energy absorbed by the PV cells into the window can generate power while most of it will be released in the form of heat then participate in the window heat transfer. Therefore, to thermal characterise the CCPC-PV window for the case of solar radiation from outside, all these absorbed solar heat terms need to be input into the CFD model to conduct the thermal modelling and the results can be found in the next section.

3.2 CFD results for thermal characterisation of the CCPC-PV window

Typical heat transfer boundary conditions (air temperature, t_{ai}, t_{ae} and surface heat transfer coefficient, h_i and h_e) specified in NFRC standard [42] for SHGC simulation as well as the solar energy absorbed by each element into the window were applied to the CFD model for thermal characterisation. This section presents the detailed thermal performance including the PV temperature, window inside surface temperature and the final updated PV efficiency for the original CCPC-PV window first, and then the performance data is presented for the CCPC-PV window with various designs.

3.2.1 Temperature profile of original CCPC-PV window

Fig. 27 shows the temperature profile of the original CCPC-PV window at 0° incident angle. Because the conduction dominates the heat transfer and the effect of the convection is small, there is no significant (air temperature, PV temperature and window inside surface temperature) temperature gradient over height. Fig. 28 shows the average PV surface temperature, average window inside surface temperature and the final updated PV efficiency at different incident angles from various planes. The average PV surface temperature gradually decreases with the increase of the incident angle and is higher at a larger plane angle for the incident angle between 40° to 80° (Fig. 28 (a)). This is because more solar energy incident on the PV surface at a larger plane angle for the incident angle between 40° to 80° (Fig. 24 (f)). The average window inside surface temperature shows the same change as that of the PV temperature across all incident angles and planes (Fig. 28 (b)). Fig. 28 (c) shows the final updated PV efficiency gradually increases with the increase of the incident angle from 0° to 90°. And it is larger for the lower plane angle when the incident angle between 40° to 80°. This tendency is opposite to the PV temperature as the PV efficiency is higher for a lower PV temperature.

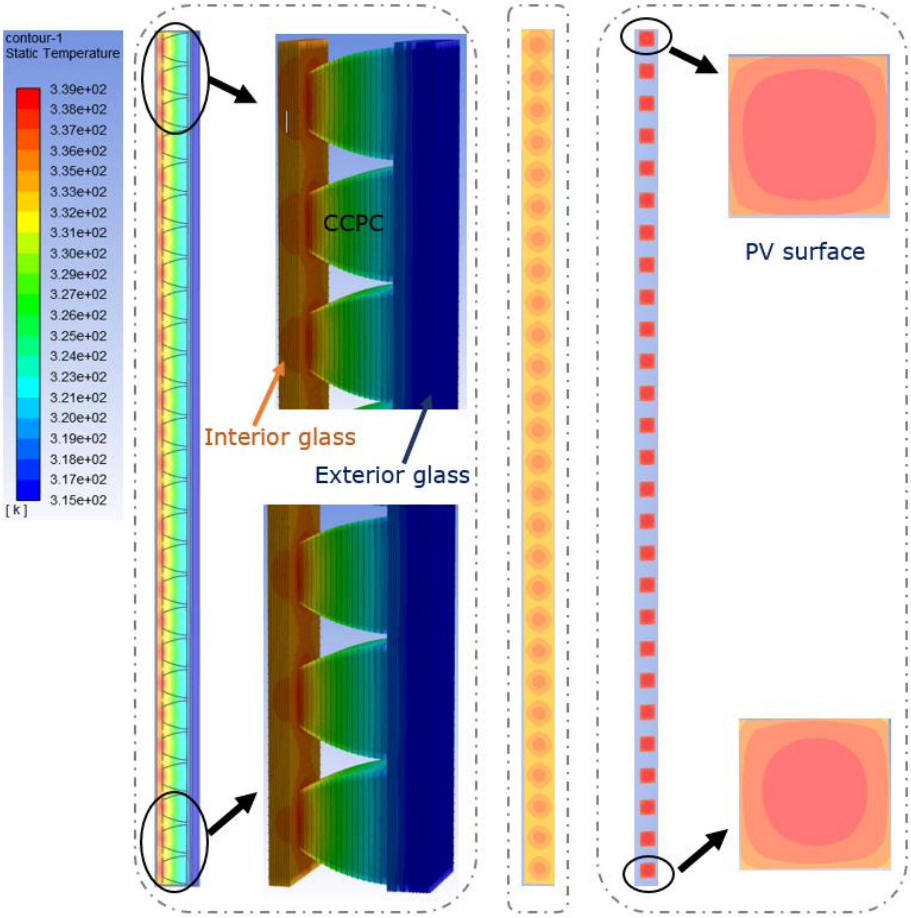

(a) (b) (c)

Fig. 27. (a) Temperature profile of the CCPC-PV window, (b) window inside surface temperature, and (c) PV surface temperature at 0° incident angle.

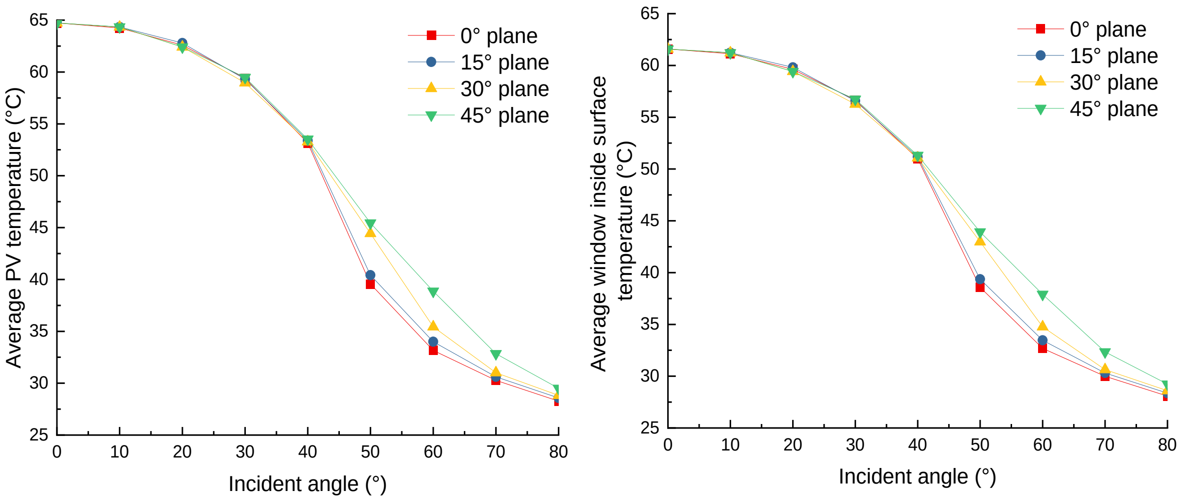

(a) (b)

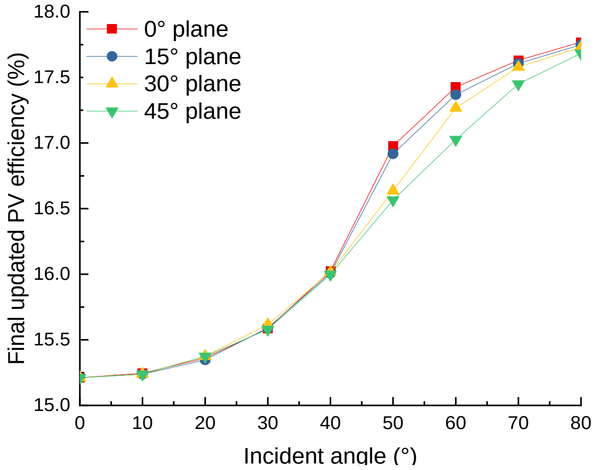

(c)

Fig. 28. (a) Average PV surface temperature, (b) average window inside surface temperature, and (c) finial updated PV efficiency.

3.2.2 Temperature profile of CCPC-PV window with various designs

Fig. 29 shows the temperature profile of the CCPC-PV window with various designs at 0° incident angle. The average PV temperature, average window inside surface temperature and final updated PV efficiency of the CCPC-PV window at different incident angles from various planes can be found in Fig. 30. As the pitch between adjacent CCPC optics increases, the average PV temperature and window inside surface temperature all decrease due to less heat released by PV power generation (Fig. 30 (a) - (d)). The final updated PV efficiency is higher for a sparser configuration because of the lower PV temperature (Fig. 30 (e) and (f)).

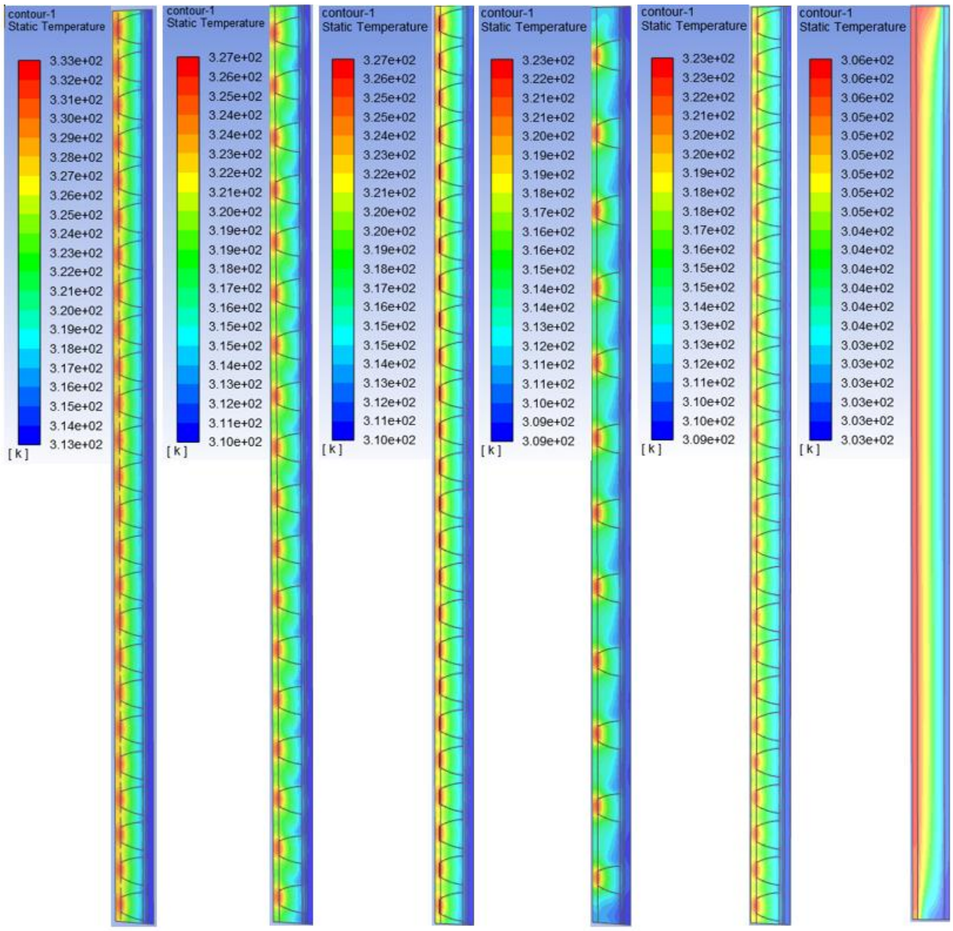

(a) (b) (c) (d) (e) (f)

Fig. 29. Temperature profile of the window with a CCPC-PV structure of (a) $D_x=D_y=5$, (b) $D_x=5$ & $D_y=15$, (c) $D_x=15$ & $D_y=5$, (d) $D_x=5$ & $D_y=30$, (e) $D_x=30$ & $D_y=5$, and (f) no CCPC-PV at 0° incident angle (D_x and D_y are horizontal and vertical pitches, mm).

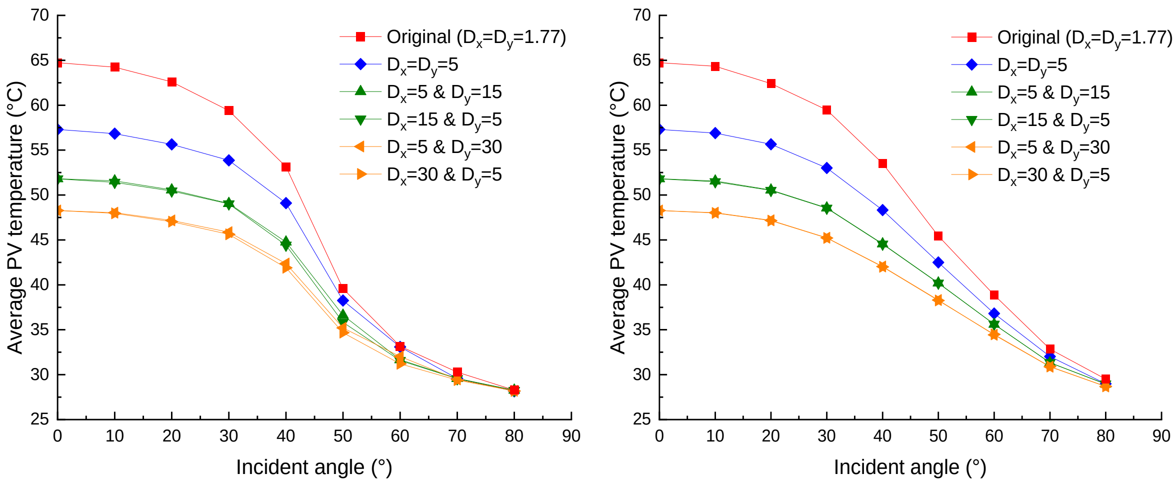

(a) 0° plane (b) 45° plane

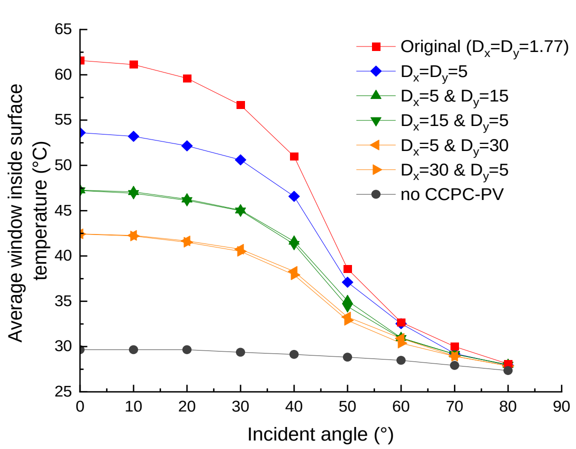

(c) 0° plane

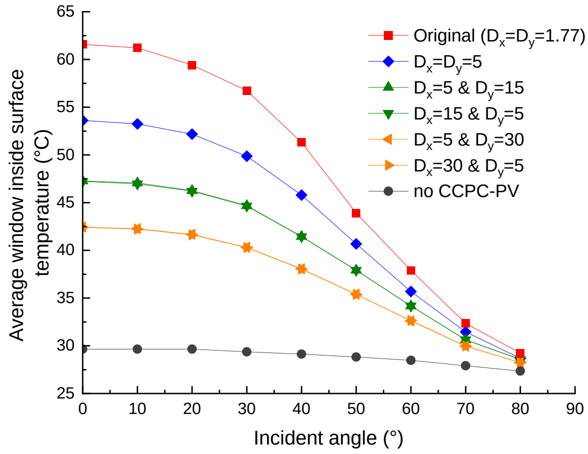

(d) 45° plane

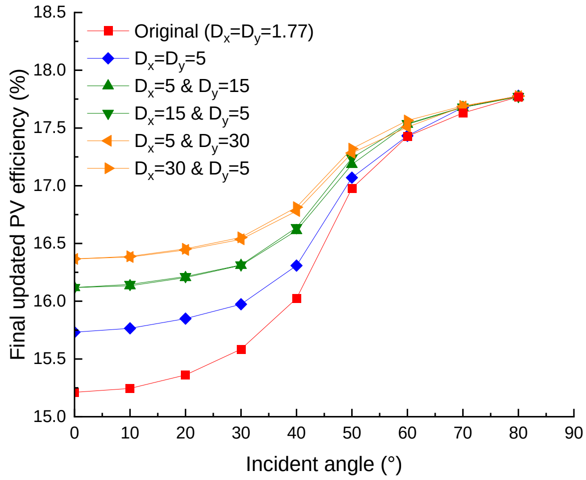

(e) 0° plane

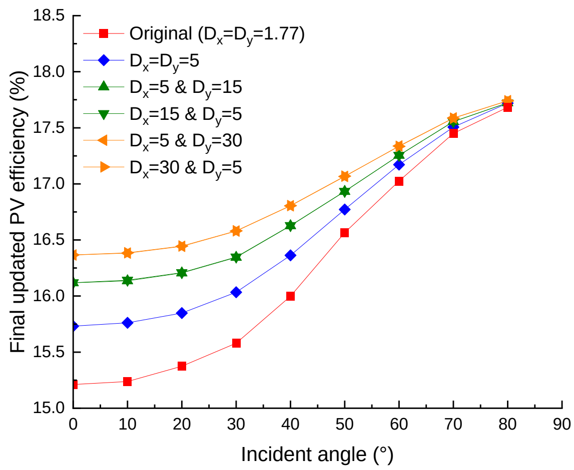

(f) 45° plane

Fig.30. (a) Average PV temperature, (c) average window inside surface temperature and (e) finial updated PV efficiency for solar rays from 0° plane and the corresponding data (b), (d), and (f) for solar rays from 45° plane (D_x and D_y are horizontal and vertical pitches, mm).

3.3 SHGC of the CCPC-PV window

As mentioned before, the SHGC value consists of the directly transmittance part and secondary heat part. The light transmittance of the CCPC-PV window and its various designs (Fig. A1 to Fig. A3 in **Appendix 1**) was investigated in our recent work by Li et al (2023) [41]. This section presents the secondary heat and SHGC of the original CCPC-PV window first. Then the data for the CCPC-PV window with various designs is presented at different incident angles from various planes.

3.3.1 SHGC of original CCPC-PV window

Fig. 31 (a) shows the secondary inward heat fraction of the SHGC under different incident angles from various planes. The proportion of secondary heat decreases gradually from 0.33 to around 0.05 as the incident angle increases from 0° to 80°. And it is lager for the higher plane angle when the incident angle is between 40° and 80°. Fig. 31 (b) shows the SHGC of the CCPC-PV window at different incident angles from various planes. The highest SHGC value (0.59) occurs at 60° incident angle from 0° plane because of the highest light transmittance (0.50).

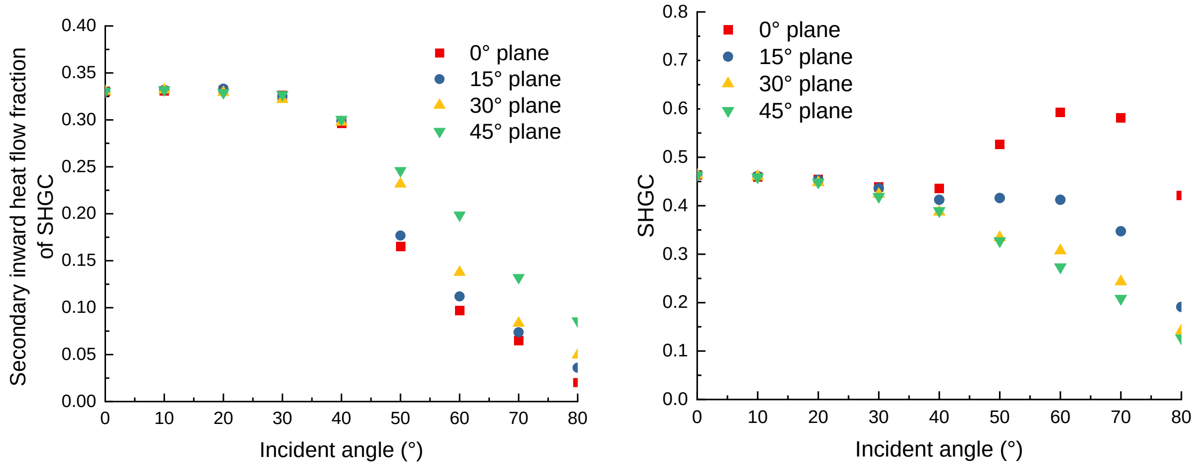

(a) (b)

Fig. 31. (a) Secondary inward heat and (b) SHGC of the CCPC-PV window.

3.3.2 SHGC of CCPC-PV window with various designs

Fig. 32 shows the secondary heat and SHGC of the CCPC-PV window with various designs. Like those with original configuration, the fraction of secondary heat is higher for solar rays from 45° plane angle especially when the incident angle ranges from 40° to 80°. As the pitch between adjacent CCPC optics increases, the fraction of secondary inward heat decreases because of the reduced amount of the PV released heat. In addition, the secondary heat of the double-glazed window is much lower than that of the CCPC-PV windows, only accounting for less than 5% of the total solar radiation incident on the exterior window surface. The SHGC value is more affected by the light transmittance (Fig. A1 to Fig. A3 in **Appendix 1**) rather than the secondary heat. For example, the SHGC value of the double-glazed window is larger than that of various CCPC-PV windows at most of incident angles from 0°and 45° plane because of its high light transmittance. And the window with a sparser CCPC-PV structure (e.g., D_x=5 mm & D_y=30 mm and D_x=30 mm & D_y=5 mm) possesses a higher SHGC because of the larger light transmittance when the incident angle is smaller than 50°. And it possesses a lower SHGC because of the lower light transmittance when the incident angle exceeds 50°.

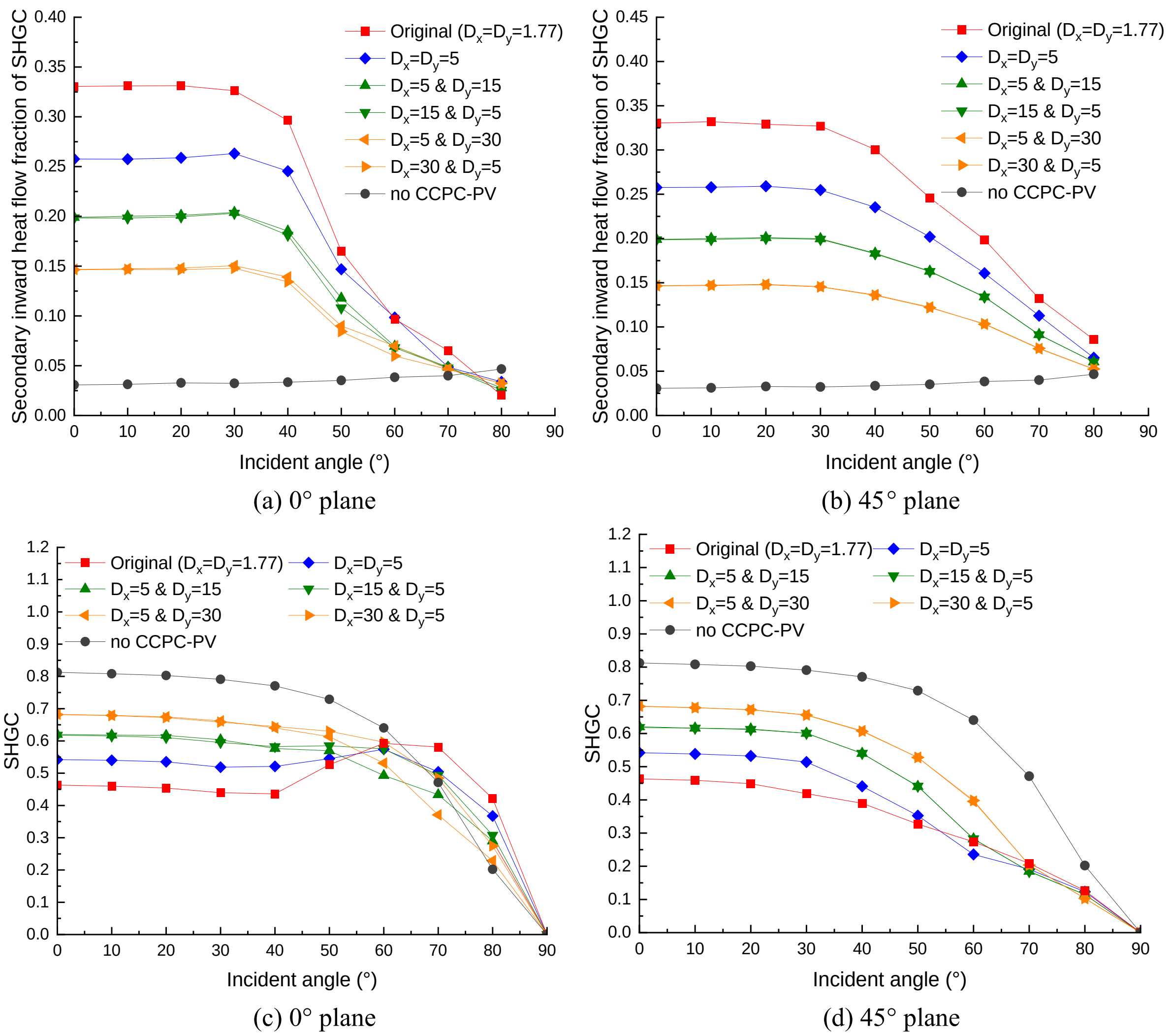

Fig. 32. (a) Secondary inward heat and (c) SHGC of CCPC-PV window for solar rays from 0° plane and the corresponding data (b) and (d) for solar rays from 45° plane (D_x and D_y are horizontal and vertical pitches, mm).

3.4 Power output of the CCPC-PV window

In this section, the power output of the original CCPC-PV window is presented first based on the above ray-tracing results of the solar energy incident on the PV surfaces and the CFD results of the PV temperature and the final updated PV efficiency. Then the results are presented for the CCPC-PV window with various designs.

3.4.1 Power output of original CCPC-PV window

Fig. 33 shows the power output of the CCPC-PV window continuously decreases from 75.91 W/m^2 to around 0.81 W/m^2 as the incident angle increases from 0° to 80°. Because more solar energy incident on the PV surface at a higher plane angle, the system output is also larger for a higher plane angle when the incident angle ranges from 40° to 80°.

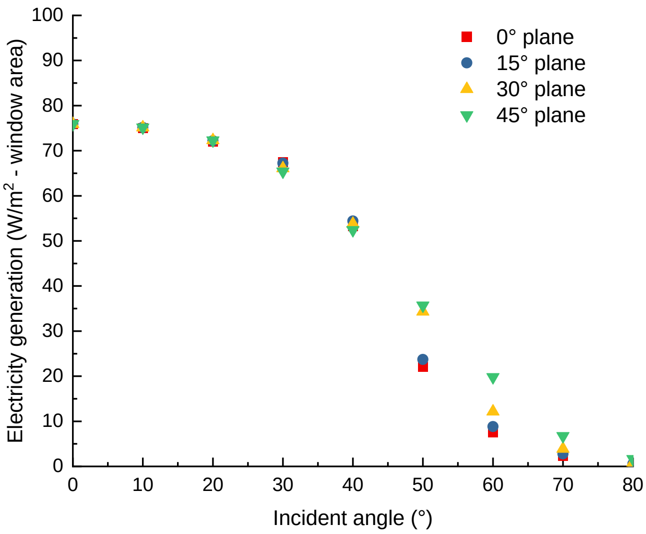

Fig. 33. Power output of the CCPC-PV window.

3.4.2 Power output of CCPC-PV window with various designs

Fig. 34 shows the power output of the CCPC-PV window with various designs. As the pitch between adjacent CCPC optics increases, the system output decreases because of the reduced number of PV cells into the window.

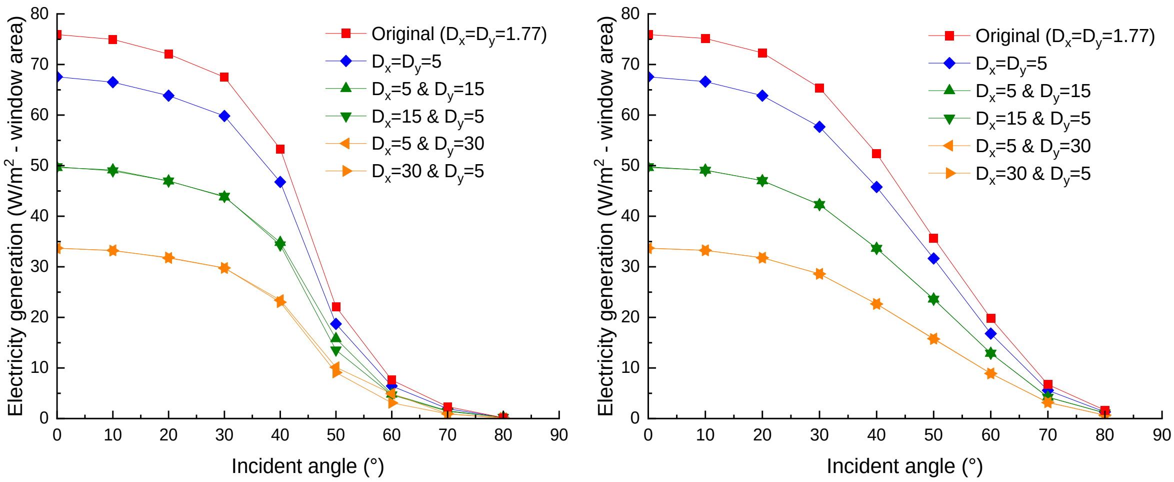

(a) 0° plane (b) 45° plane

Fig. 34. Power output of the CCPC-PV window with various designs (D_x and D_y are horizontal and vertical pitches, mm) for rays from (a) 0° plane angle and (b) 45° plane angle.

4. Summary of the performance of CCPC-PV window

This section summarises previous investigations of the thermal, optical, and electrical performance of the CCPC-PV window and its various designs. The overall assessment includes the U-value (EN673 [53]), SHGC (NFRC [42]), light transmittance and power output. Among these parameters, the thermal insulation property (U-value) and light transmittance of the

CCPC-PV window and its various designs have been investigated in our recent work by Li et al (2023) [41] and the results are also listed in Table 11. For a clear traditional double-glazed window, it was reported that it has always incurred oversupplied daylight and solar heat in summer due to high transmittance when applying it to a south-facing façade [54]. From Table 11, it can be seen that the integration of various CCPC-PV structures between two glass panes contributes to improved thermal, optical, and electrical performance. This includes reduced U-value and SHGC, decreased light transmittance, and increased power generation. All of these factors demonstrate the potential benefits of using CCPC-PV windows for energy-efficient buildings. The windows with original CCPC-PV structure (D_x=D_y=1.77 mm) and structure of D_x=D_y=5 mm have lower U-values and higher electricity generations. However, the sunlight and solar heat that can transmit through the window system are limited. Therefore, it is more suitable for the building application with a large Window-to-Wall-Ratio (WWR). The low light transmittance and SHGC value can lead to a modest indoor luminous environment and sufficient solar heat gain in winter. For building with a small WWR application, the CCPC-PV window should be designed with a larger horizontal pitch, such as 15 and 30 mm, to satisfy the indoor illuminance requirement and ensure the sufficient solar heat meanwhile provide advanced thermal insulation performance and additional power output.

Table 11. Overall assessment for the thermal, optical, and electrical performance of the double-glazed window containing various CCPC-PV structures (D_x and D_y are horizontal and vertical pitches, mm) based on EN673 standard for calculating the U-value, and NFRC standard for calculating the SHGC, light transmittance and power output at normal incidence condition.

CCPC-PV structure	Original, D_x=D_y=1.77	D_x=D_y =5	D_x=5 & D_y=15	D_x=5 & D_y=30	D_x=15 & D_y=5	D_x=30 & D_y=5	No CCPC-PV
U-value (W/m^2·K)	2.575	2.566	2.657	2.573	2.706	2.575	2.805
Light transmittance (-)	0.133	0.284	0.421	0.536	0.420	0.535	0.782
SHGC (-)	0.463	0.542	0.620	0.683	0.618	0.682	0.813
Power output (W/m^2 - window area)	75.914	67.556	49.644	33.650	49.769	33.708	-

5. Conclusions

This study has provided a detailed procedure for development of a comprehensive model to investigate the optical, thermal and electrical performance of a complex PV window system (e.g., CCPC-PV window) using a CFD combined ray-tracing method. The performance of the CCPC-PV window and its various designs were compared to those of a similar double-glazed system. Based on the findings, the following conclusions are drawn:

1) The developed comprehensive model would be sufficient to predict the optical, thermal and electrical performance of a complex PV window system with an error of less than 4%.

2) For original CCPC-PV window (1.77 mm-pitch), the maximum PV temperature and window inside surface temperature can reach 64.73 °C and 61.58 °C under NFRC standard and the corresponding PV efficiency is 15.21%.

3) Increasing the horizontal/vertical pitch between adjacent CCPC optics from 5 mm to 30 mm leads to a decrease in the average PV temperature from 58 °C to 48 °C at 0° incident angle, and a decrease in the average inside surface temperature from 54 °C to 43 °C. At the same time, the updated PV efficiency increases from 15.7% to 16.4%.

4) The SHGC of the CCPC-PV window is primarily influenced by the light transmittance rather than the secondary heat. Consequently, windows with higher light transmittance, such as those with sparser CCPC-PV structures of D_x=5 mm & D_y=30 mm and D_x=30 mm & D_y=5 mm, have the maximum SHGC value (0.68) at 0° incident angle.

5) The window with a CCPC-PV structure of D_x=15 mm, 30 mm & D_y=5 mm provides better thermal insulation (with a smaller U-value) than those with a structure of D_x=5 mm & D_y=15 mm, 30 mm. These windows exhibit similar optical transmittance, SHGC value, and power output.

6) The CCPC-PV window and its various designs all exhibit advanced thermal properties (lower U-value and SHGC), optical properties (lower light transmittance) and additional power output compared to a similar structured double-glazed system.

The individual parameters obtained in this study can provide an indication of the advanced optical, thermal and electrical performance of various CCPC-PV windows in comparison to a similarly structured double-glazed window. However, these parameters are insufficient to fully evaluate the impact of CCPC-PV windows on building energy and daylight performance. When this window is installed on a building, its optical transmittance, SHGC, and system output all change according to the varying solar positions throughout the year, significantly affecting building energy consumption. Therefore, a building simulation model that takes into account all these dynamic properties should be developed in the future to comprehensively evaluate the energy savings and daylighting benefits that can be achieved through the use of CCPC-PV windows in a building.

Acknowledgements

This work was supported by the Faculty of Engineering, University of Nottingham and the China Scholarship Council through a joint PhD studentship awarded to Xue Li. This work was also supported by the Engineering and Physical Sciences Research Council, UK [grant number EP/S030786/1].

Appendix 1

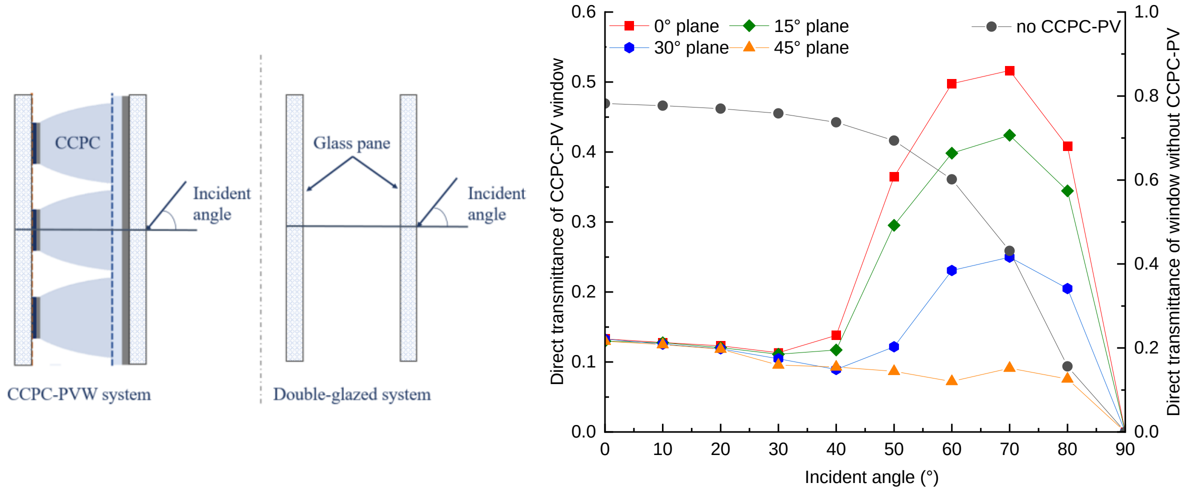

(a) (b)

Fig. A1. (a) Incident angle (θ) of the window and (b) light transmittance of the original CCPC-PV window and double-glazed window.

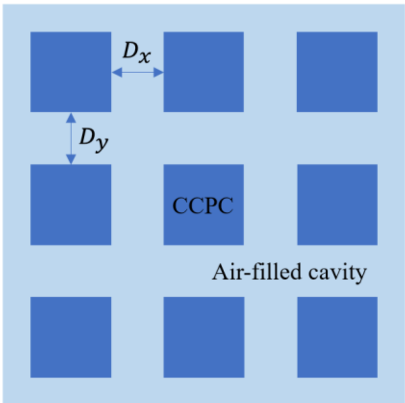

(a)

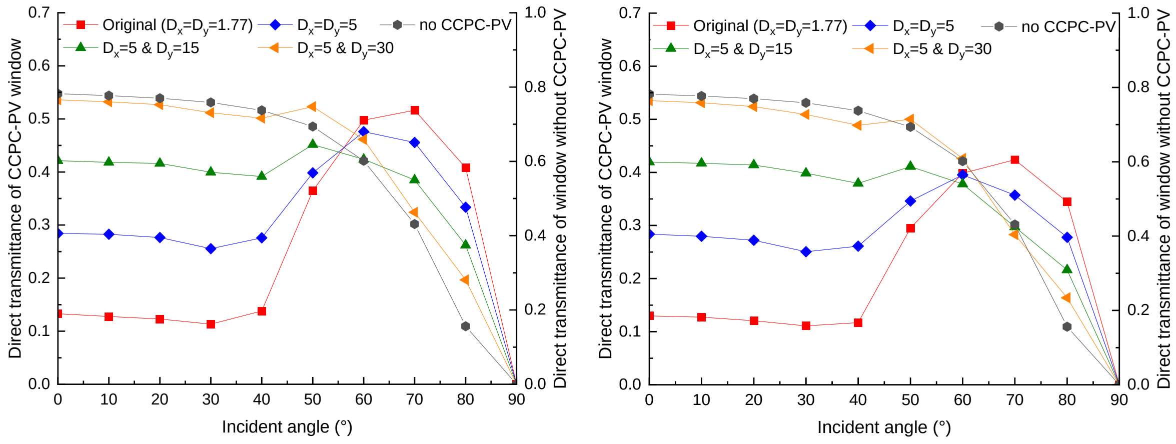

(b) (c)

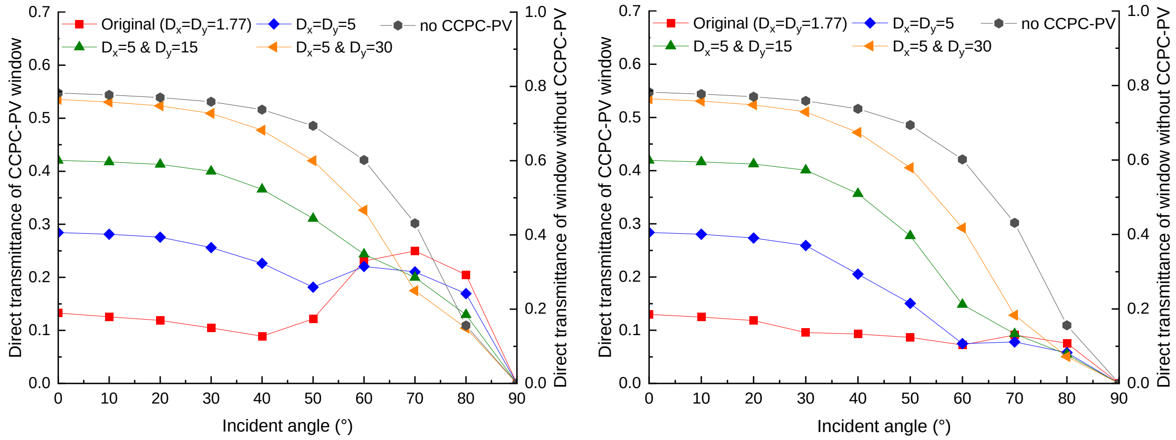

(d) (e)

Fig. A2. (a) Horizontal pitch (D_x, mm) and vertical pitch (D_y, mm) between adjacent CCPC optics, light transmittance of the double-glazed window containing various CCPC-PV structures for rays from (b) 0°, (c) 15°, (d) 30° and (e) 45° planes.

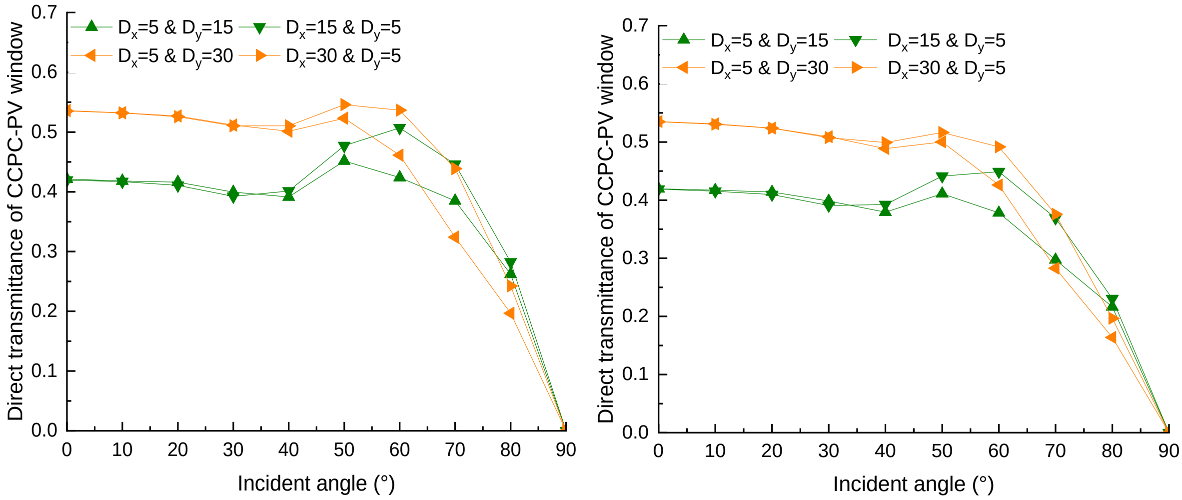

(a) (b)

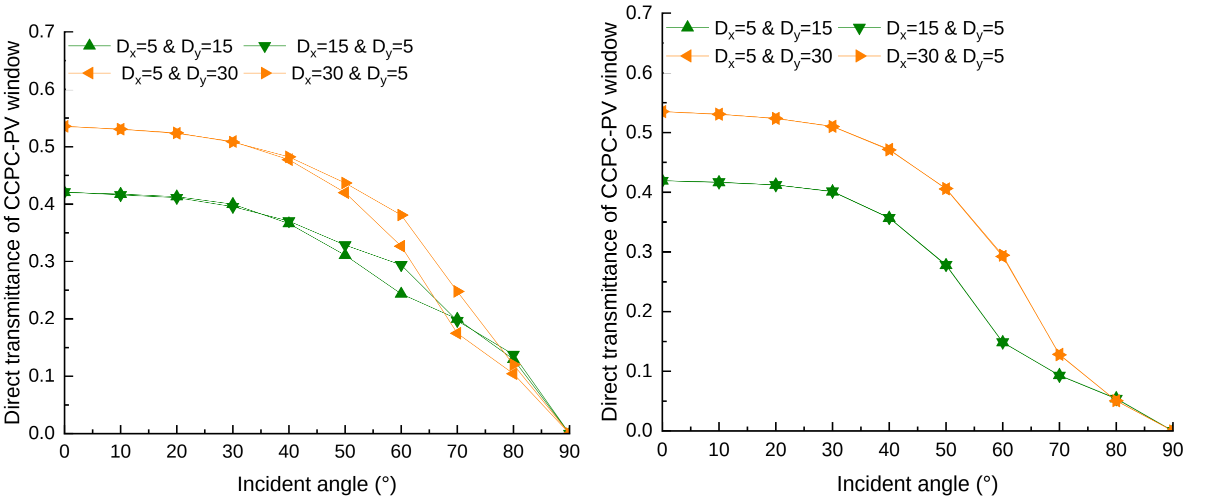

(c) (d)

Fig. A3. Comparison of the light transmittance of the double-glazed window containing a CCPC-PV structure of D_x=5 & D_y=15, 30 and D_x=15, 30 & D_y=5 for rays from (a) 0°, (b) 15°, (c) 30°, and (d) 45° planes (D_x and D_y are horizontal and vertical pitches, mm).

Reference

1. Gosselin, L. and J.-M. Dussault, *Correlations for glazing properties and representation of glazing types with continuous variables for daylight and energy simulations.* Solar Energy, 2017. **141**: p. 159-165.
2. Field, E. and A. Ghosh, *Energy assessment of advanced and switchable windows for less energy-hungry buildings in the UK.* Energy, 2023. **283**: p. 128999.
3. Harmathy, N., Z. Magyar, and R. Folić, *Multi-criterion optimization of building envelope in the function of indoor illumination quality towards overall energy performance improvement.* Energy, 2016. **114**: p. 302-317.
4. Xu, Y., et al., *A multi-objective optimization method based on an adaptive meta-model for classroom design with smart electrochromic windows.* Energy, 2022. **243**: p. 122777.
5. Aguilar-Santana, J.L., et al., *Review on window-glazing technologies and future prospects.* International Journal of Low-Carbon Technologies, 2020. **15**(1): p. 112-120.
6. Pu, J., C. Shen, and L. Lu, *Investigating the annual energy-saving and energy-output behaviors of a novel liquid-flow window with spectral regulation of ATO nanofluids.* Energy, 2023: p. 129111.
7. Ghosh, A., *Investigation of vacuum-integrated switchable polymer dispersed liquid crystal glazing for smart window application for less energy-hungry building.* Energy, 2023. **265**: p. 126396.
8. Mesloub, A., et al., *Assessment of the overall energy performance of an SPD smart window in a hot desert climate.* Energy, 2022. **252**: p. 124073.
9. Tällberg, R., et al., *Comparison of the energy saving potential of adaptive and controllable smart windows: A state-of-the-art review and simulation studies of thermochromic, photochromic and electrochromic technologies.* Solar Energy Materials and Solar Cells, 2019. **200**: p. 109828.
10. Akram, M.W., et al., *Global technological advancement and challenges of glazed window, facade system and vertical greenery-based energy savings in buildings: A comprehensive review.* Energy and Built Environment, 2021.
11. Sun, Y., et al., *Thermal evaluation of a double glazing façade system with integrated Parallel Slat Transparent Insulation Material (PS-TIM).* Building and Environment, 2016. **105**: p. 69-81.
12. Khaled Mohammad, A. and A. Ghosh, *Exploring energy consumption for less energy-hungry building in UK using advanced aerogel window.* Solar Energy, 2023. **253**: p. 389-400.
13. Hassani, A.R., et al., *Evaluation of the solar heat gain coefficient of innovative aerogel glazing systems: Experimental campaigns and numerical results.* Journal of Building Engineering, 2022. **62**: p. 105354.

14. Wang, M., et al., *Comparison of energy performance between PV double skin facades and PV insulating glass units.* Applied Energy, 2017. **194**: p. 148-160.
15. Abolghasemi Moghaddam, S., N. Simões, and M. Gameiro da Silva, *Review of the experimental methods for evaluation of windows' solar heat gain coefficient: From standardized tests to new possibilities.* Building and Environment, 2023. **242**: p. 110527.
16. Kuhn, T.E., *Calorimetric determination of the solar heat gain coefficient g with steady-state laboratory measurements.* Energy and Buildings, 2014. **84**: p. 388-402.
17. Marinoski, D.L., et al., *Improvement of a measurement system for solar heat gain through fenestrations.* Energy and Buildings, 2007. **39**(4): p. 478-487.
18. Peng, J., L. Lu, and H. Yang, *An experimental study of the thermal performance of a novel photovoltaic double-skin facade in Hong Kong.* Solar Energy, 2013. **97**: p. 293-304.
19. Peng, J., et al., *Comparative study of the thermal and power performances of a semi-transparent photovoltaic façade under different ventilation modes.* Applied Energy, 2015. **138**: p. 572-583.
20. Nie, Z., et al., *Adaptive Façades Strategy: An architect-friendly computational approach based on co-simulation and white-box models for the early design stage.* Energy and Buildings, 2023. **296**: p. 113320.
21. Wang, C., et al., *Design and performance investigation of a novel double-skin ventilated window integrated with air-purifying blind.* Energy, 2022. **254**: p. 124476.
22. Martín-Chivelet, N., et al., *Building-Integrated Photovoltaic (BIPV) products and systems: A review of energy-related behavior.* Energy and Buildings, 2022. **262**: p. 111998.
23. Peng, J., et al., *Numerical investigation of the energy saving potential of a semi-transparent photovoltaic double-skin facade in a cool-summer Mediterranean climate.* Applied Energy, 2016. **165**: p. 345-356.
24. *ISO, 15099:* Thermal performance of windows, doors and shading devices --Detailed calculations. 2003.
25. DIN, E., *410: 2011-04 (2011) Glas im Bauwesen–Bestimmung der lichttechnischen und strahlungsphysikalischen Kenngrößen von Verglasungen.* Deutsche Fassung EN, 2011. **410**.
26. Baenas, T. and M. Machado, *On the analytical calculation of the solar heat gain coefficient of a BIPV module.* Energy and Buildings, 2017. **151**: p. 146-156.
27. Chen, F., et al., *Solar heat gain coefficient measurement of semi-transparent photovoltaic modules with indoor calorimetric hot box and solar simulator.* Energy and Buildings, 2012. **53**: p. 74-84.

28. Villalba, A., et al., *Hot-cool box calorimetric determination of the solar heat gain coefficient and the U-value of internal shading devices.* Energy Efficiency, 2017. **10**(6): p. 1553-1571.
29. *ISO,19467: Thermal performance of windows and doors — Determination of solar heat gain coefficient using solar simulator.* 2017.
30. Simmler, H. and B. Binder, *Experimental and numerical determination of the total solar energy transmittance of glazing with venetian blind shading.* Building and Environment, 2008. **43**(2): p. 197-204.
31. Kersken, M., *Method for the climate-independent determination of the solar heat gain coefficient (SHGC; g-value) of transparent façade and membrane constructions from in situ measurements.* Energy and Buildings, 2021. **239**: p. 110866.
32. Craig, K.J., et al., *Using CFD and ray tracing to estimate the heat losses of a tubular cavity dish receiver for different inclination angles.* Solar Energy, 2020. **211**: p. 1137-1158.
33. Craig, K.J., J. Marsberg, and J.P. Meyer, *Combining ray tracing and CFD in the thermal analysis of a parabolic dish tubular cavity receiver.* AIP Conference Proceedings, 2016. **1734**(1): p. 030009.
34. Li, Z., et al., *Study on the radiation flux and temperature distributions of the concentrator–receiver system in a solar dish/Stirling power facility.* Applied Thermal Engineering, 2011. **31**(10): p. 1780-1789.
35. Wang, W., et al., *Conjugate heat transfer analysis of an impinging receiver design for a dish-Brayton system.* Solar Energy, 2015. **119**: p. 298-309.
36. Zhang, Y., et al., *Combined optics and heat transfer numerical model of a solar conical receiver with built-in helical pipe.* Energy, 2020. **193**: p. 116775.
37. Daabo, A.M., et al., *Numerical investigation of pitch value on thermal performance of solar receiver for solar powered Brayton cycle application.* Energy, 2017. **119**: p. 523-539.
38. Du, S., et al., *Pore-scale numerical simulation of fully coupled heat transfer process in porous volumetric solar receiver.* Energy, 2017. **140**: p. 1267-1275.
39. Demanega, I.e.a., *CFD and Ray Tracing to Evaluate the Thermal Performance of Complex Fenestration Systems* 2018.
40. Baig, H., et al., *Numerical modelling and experimental validation of a low concentrating photovoltaic system.* Solar Energy Materials and Solar Cells, 2013. **113**: p. 201-219.
41. Li, X. et al (2023). Comprehensive investigation of a Building Integrated Crossed Compound Parabolic Concentrator Photovoltaic window System: Thermal, Optical and Electrical performance. Manuscript submitted to 'Renewable Energy' for publication.

42. *NFRC 200-2014: Procedure for Determining Fenestration Product Solar Heat Gain Coefficient and Visible Transmittance at Normal Incidence. 2014.*
43. Baig, H., et al., *Performance analysis of a dielectric based 3D building integrated concentrating photovoltaic system.* Solar Energy, 2014. **103**: p. 525-540.
44. Shanks, K., et al., *An experimental analysis of the optical, thermal and power to weight performance of plastic and glass optics with AR coatings for embedded CPV windows.* Solar Energy Materials and Solar Cells, 2019. **200**: p. 110027.
45. Liu, X. and Y. Wu, *Experimental characterisation of a smart glazing with tuneable transparency, light scattering ability and electricity generation function.* Applied Energy, 2021. **303**: p. 117521.
46. Sun, Y., et al., *Thermal evaluation of a double glazing façade system with integrated Parallel Slat Transparent Insulation Material (PS-TIM)*. Vol. 105. 2016.
47. Wu, Y., et al., *Smart solar concentrators for building integrated photovoltaic façades.* Solar Energy, 2016. **133**: p. 111-118.
48. Müllejans, H. and E. Salis, *Linearity of photovoltaic devices: quantitative assessment with N-lamp method.* Measurement Science and Technology, 2019. **30**(6): p. 065008.
49. Ferrer-Rodríguez, J.P., et al., *Development, indoor characterisation and comparison to optical modelling of four Fresnel-based high-CPV units equipped with refractive secondary optics.* Solar Energy Materials and Solar Cells, 2018. **186**: p. 273-283.
50. Mammo, E.D., N. Sellami, and T.K. Mallick, *Performance analysis of a reflective 3D crossed compound parabolic concentrating photovoltaic system for building façade integration.* Progress in Photovoltaics: Research and Applications, 2013. **21**(5): p. 1095-1103.
51. Ren, X.-H., et al., *Thermal driven natural convective flows inside the solar chimney flush-mounted with discrete heating sources: Reversal and cooperative flow dynamics.* Renewable Energy, 2019. **138**: p. 354-367.
52. Rath, S. and S.K. Dash, *Numerical study of laminar and turbulent natural convection from a stack of solid horizontal cylinders.* International Journal of Thermal Sciences, 2020. **148**: p. 106147.
53. *BS EN 673:2011: Glass in building. Determination of thermal transmittance (U value). Calculation method*. 2011, British Standards Institute.
54. Qiu, C. and H. Yang, *Daylighting and overall energy performance of a novel semi-transparent photovoltaic vacuum glazing in different climate zones.* Applied Energy, 2020. **276**: p. 115414.